

Structure Solution from Powder Diffraction Data

SSPD'03

September 14-19, 2003

Congress Center Academia, Stara Lesna, Slovakia

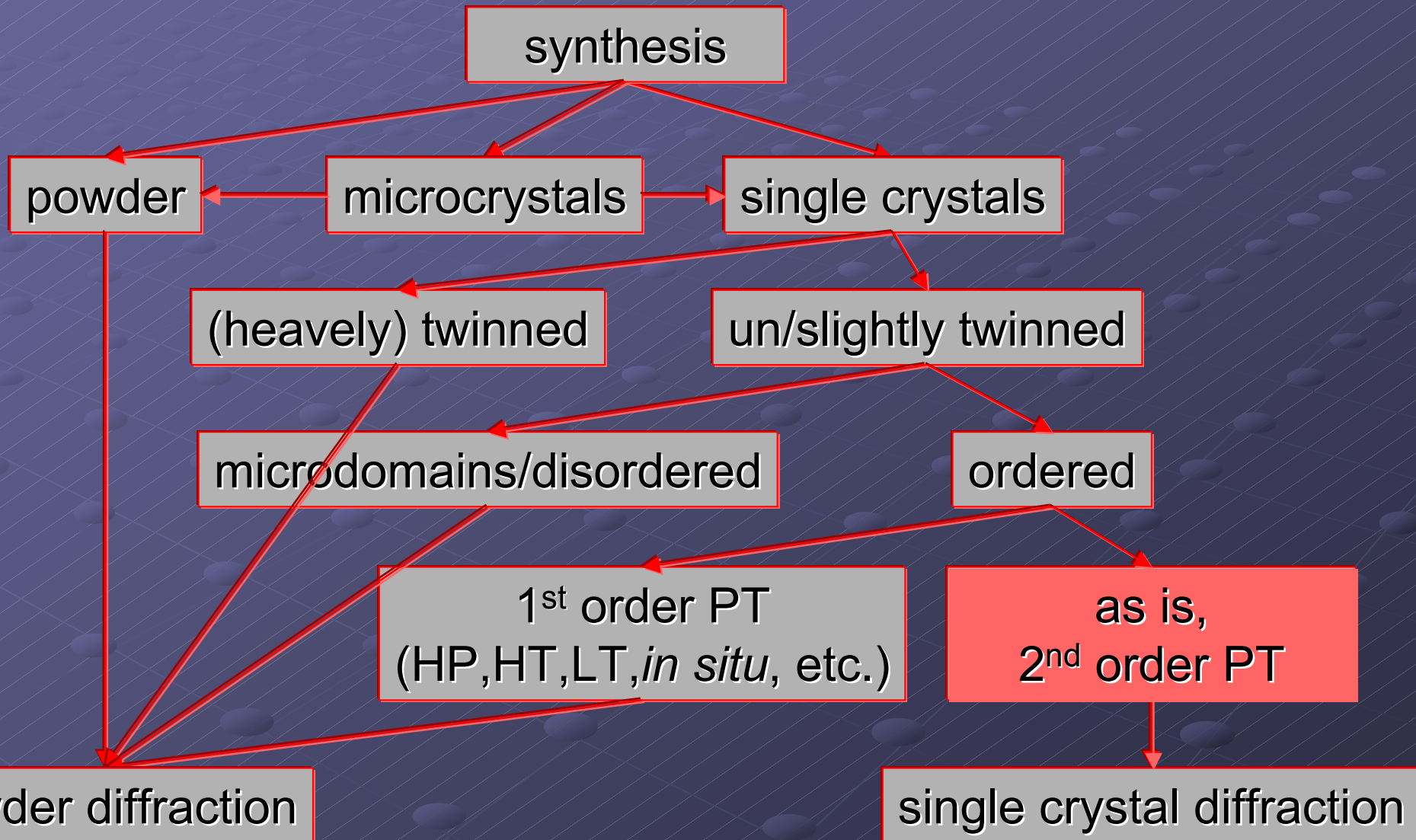
High Resolution Powder Diffraction: An indispensable tool in modern solid state chemistry

Robert E. Dinnebier

Max-Planck-Institute for Solid State Research

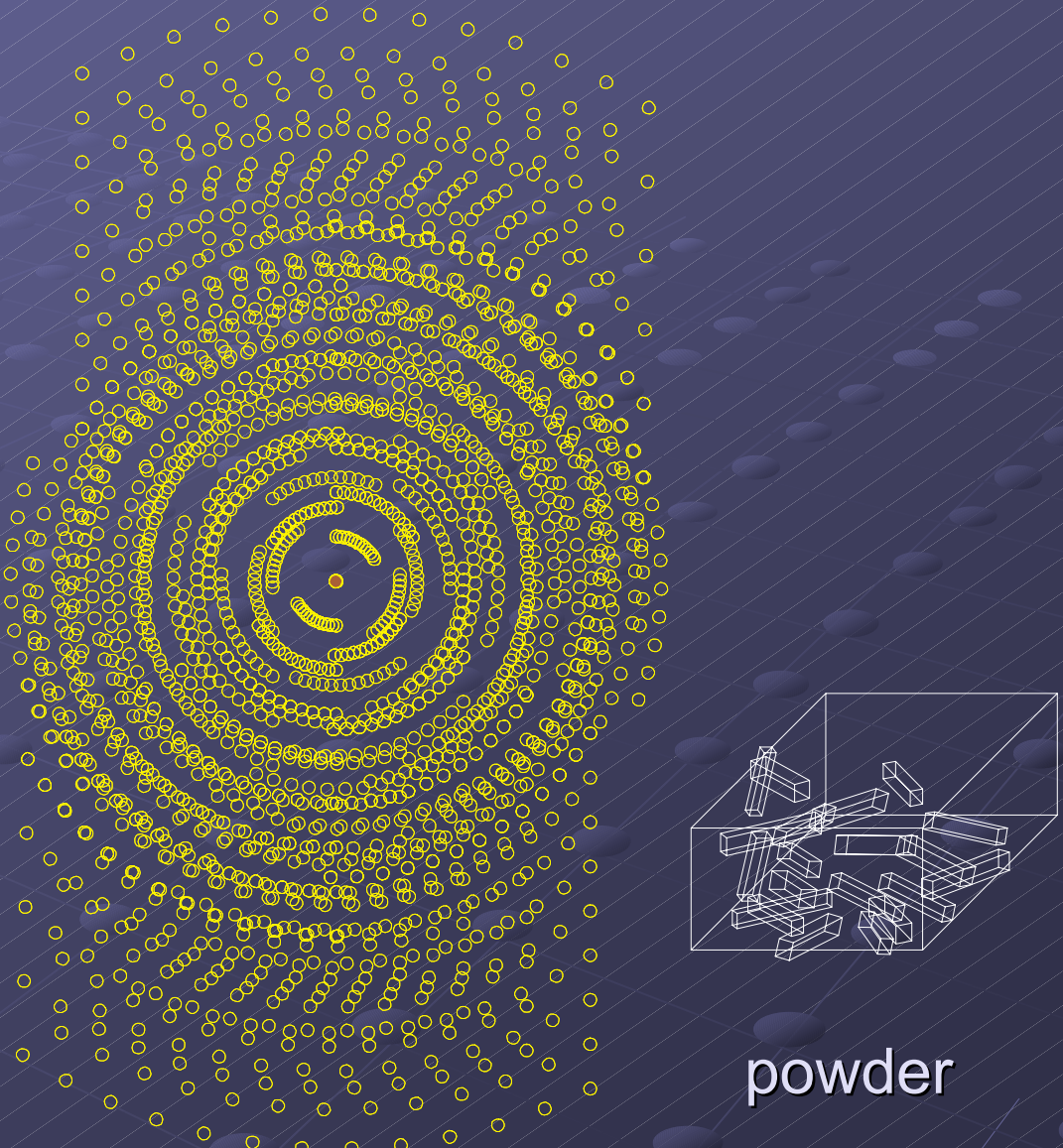
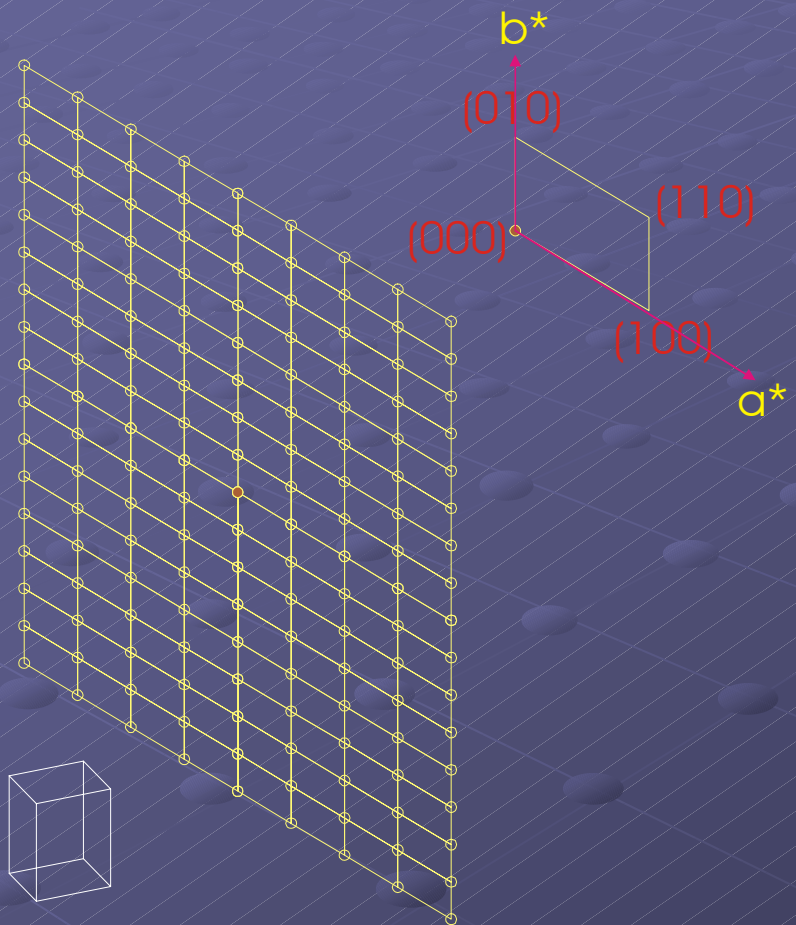
Stuttgart, Germany

Why Powder Diffraction ?



single crystal \leftrightarrow powder

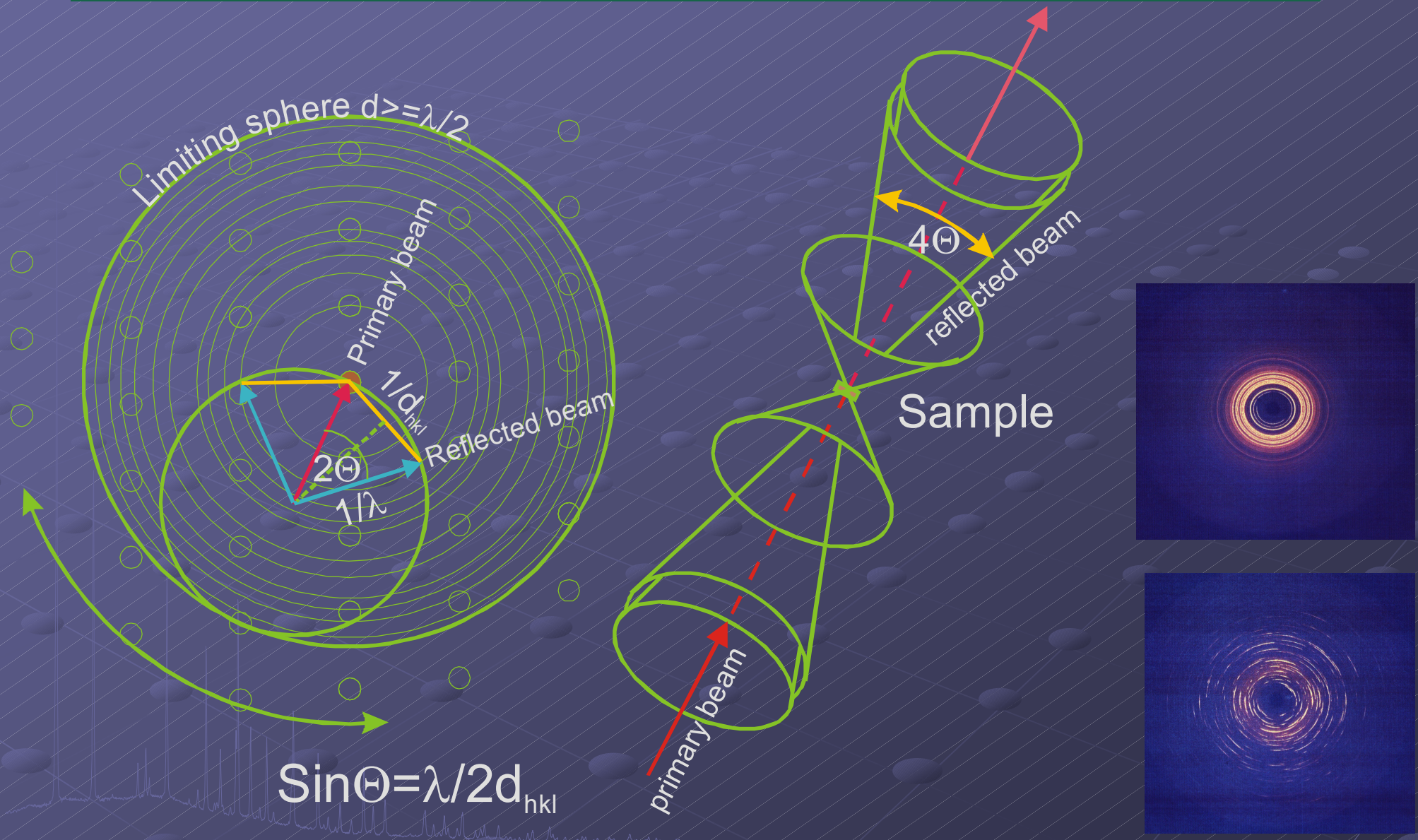
2-dim reciprocal lattice



single crystal

powder

Powder diffraction – reciprocal & real space



the problem of powder diffraction

Powder: Single crystal reciprocal lattice is smeared into spherical shells

→Projection of the 3-dim reciprocal space onto the one dimensional 2Θ -axis
reflections at equal d-spacings contribute to the same powder diffraction line

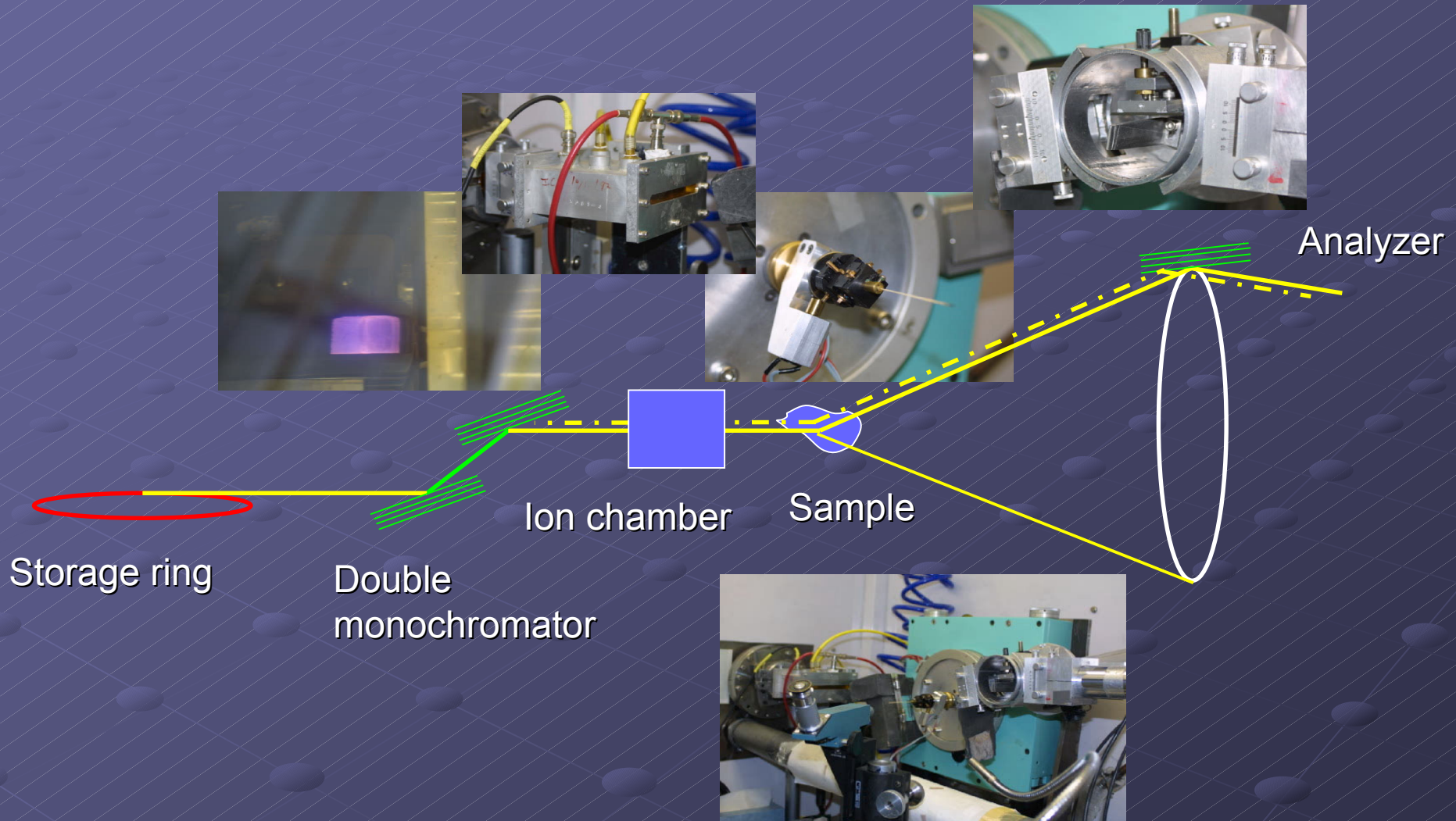
$$\vec{Q} \Rightarrow |Q|$$

→Different degrees of overlap:

- multiplicity (min. 2 max 48) (e.g. 100, -100, 010, 0-10, 001, 00-1 in the cubic case)
- systematical (e.g. 511, 333 in the cubic case)
- accidental (depending on lattice parameters and scattering angle)

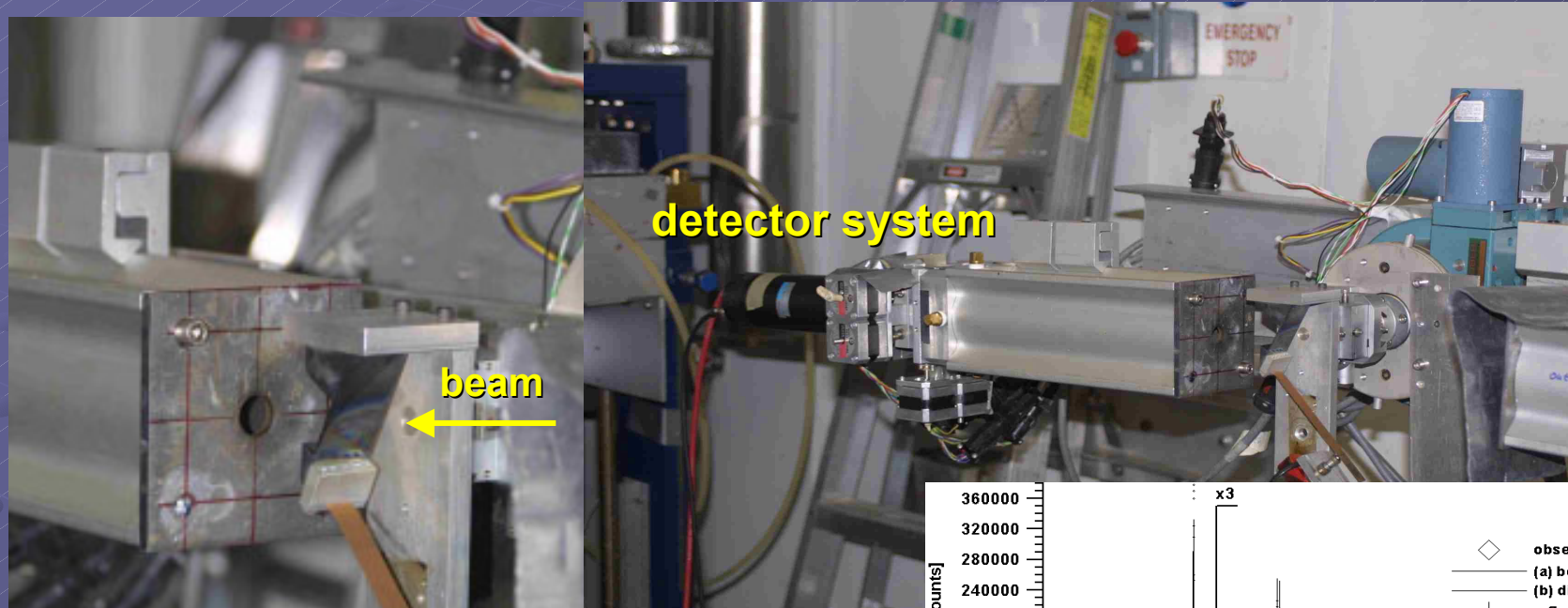
⇒The intensities and FWHM's of individual reflections can often not be determined with sufficient accuracy

Parallel beam diffraction instrument at beamline X3B1 at the National Synchrotron Light Source (NSLS)

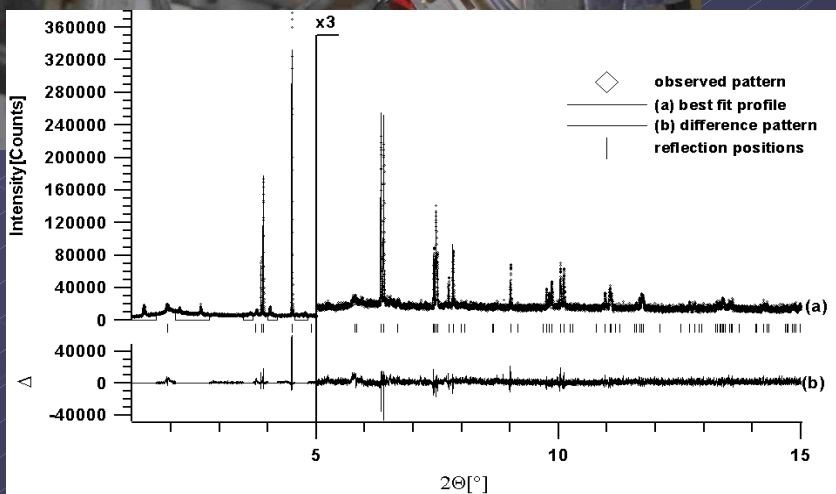


(No peak shift from sample displacement, transparency. No distortion from imperfect focus)

Alternative: high resolution, high energy diffractometer

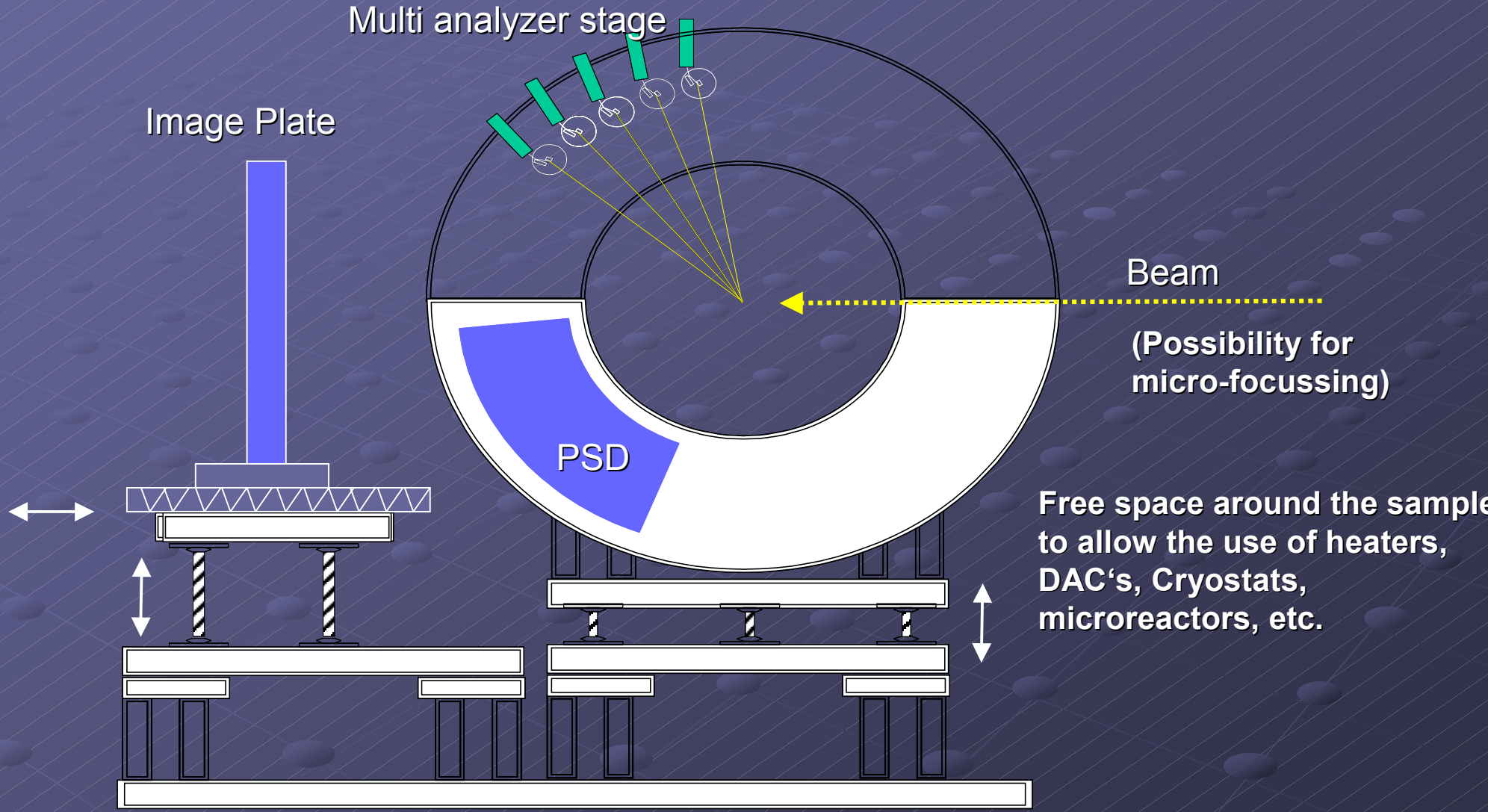


bent Laue monochromator



Na_3BiO_4 , X17B1, NSLS, $\lambda = 0.18528 \text{ \AA}$

Design of a multi purpose powder diffractometer

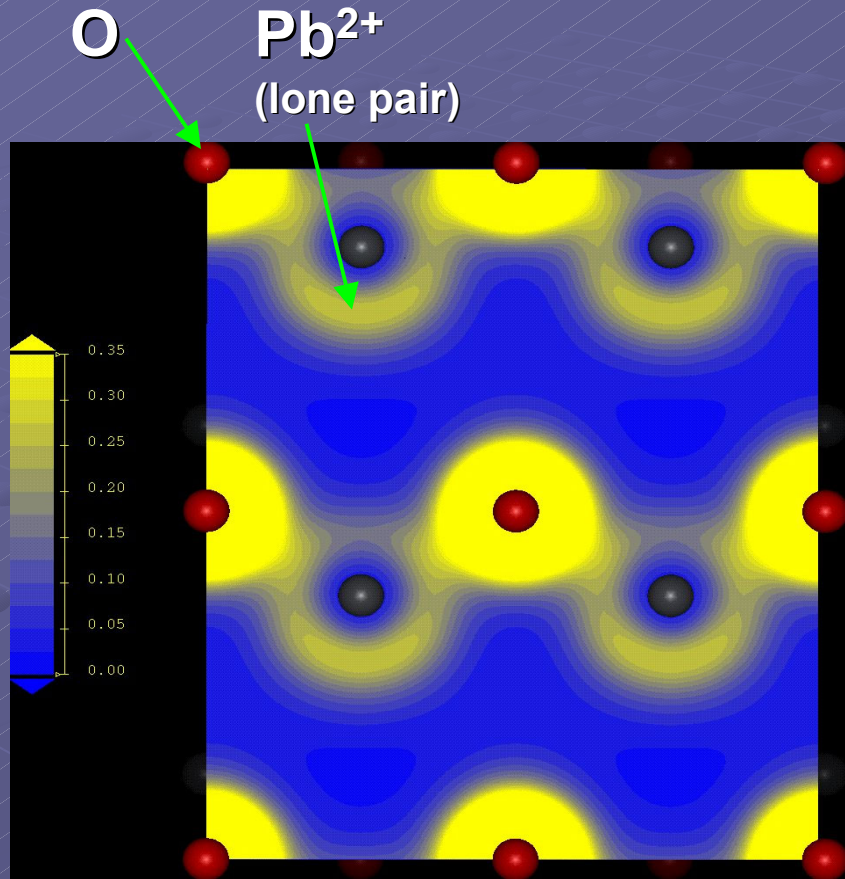


Bulk modulus and high pressure crystal structures of Pb_3O_4 (Minium)

Dinnebier, Carlson, Hanfland & Jansen,
American Mineralogist 2003, in press

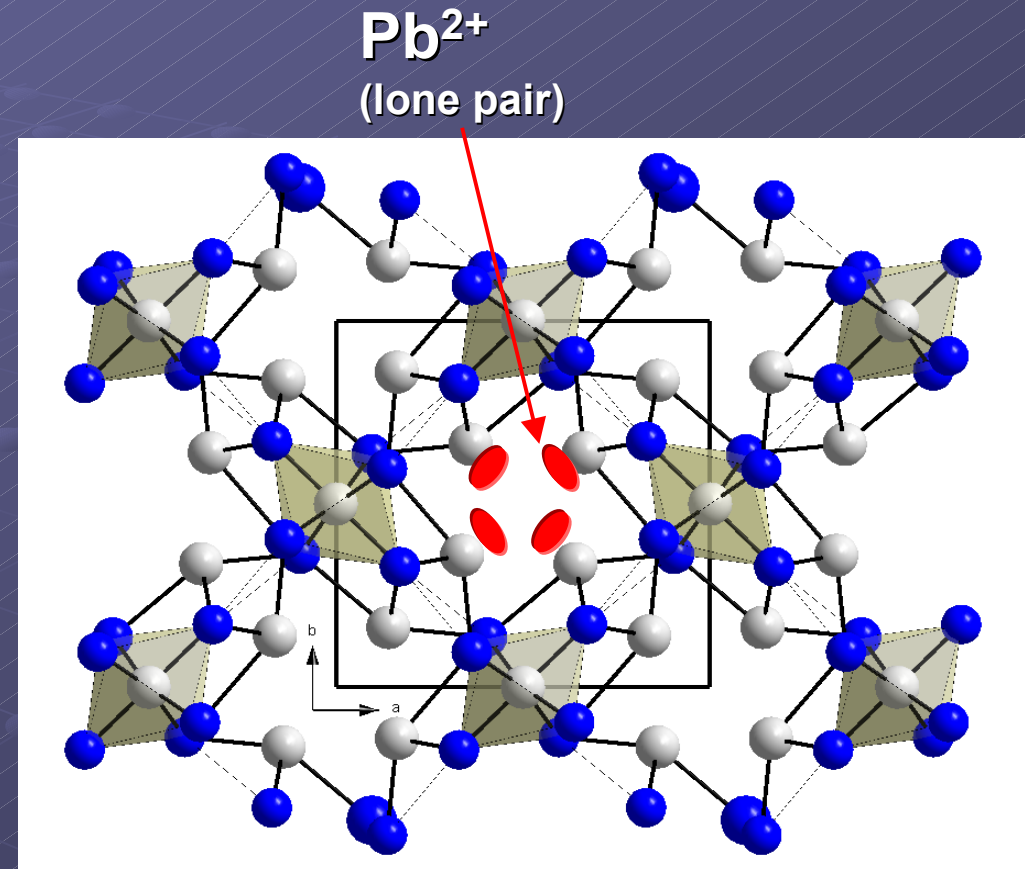


The lone pair of Pb^{2+}



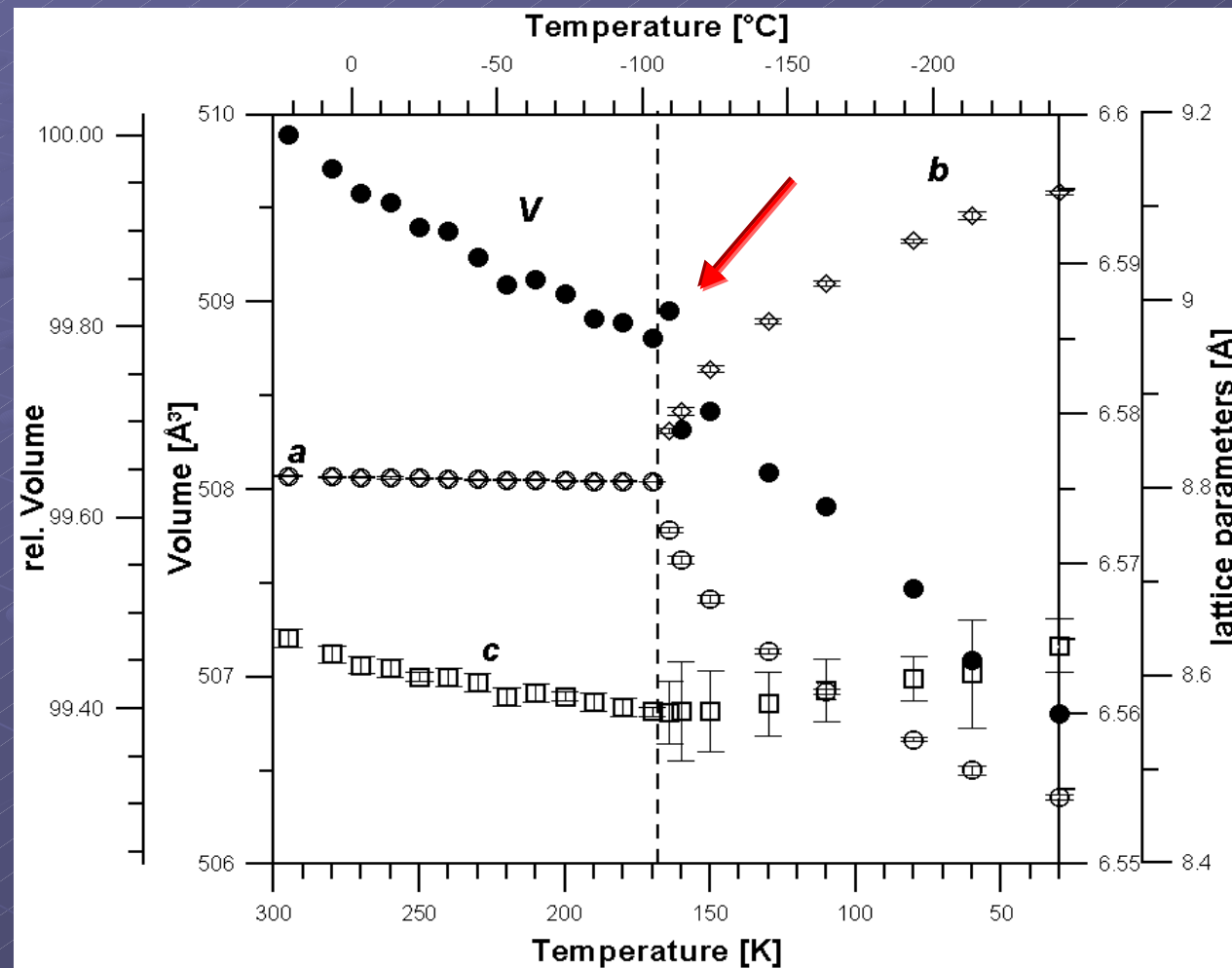
Ab initio calculations of the origin of
the distortion of $\alpha\text{-PbO}$ (Pb^{+II}O)

Watson, Parker & Kresse,
Phys. Rev. B59, 1999, 8481-8486



Pb_3O_4 ($\text{Pb}^{+IV}\text{Pb}^{+II}_2\text{O}_4$) at ambient conditions

Pb_3O_4 at low temperature



Lattice parameters and (rel.) volume of Minium in dependence of temperature (Garnier et al., 1976)

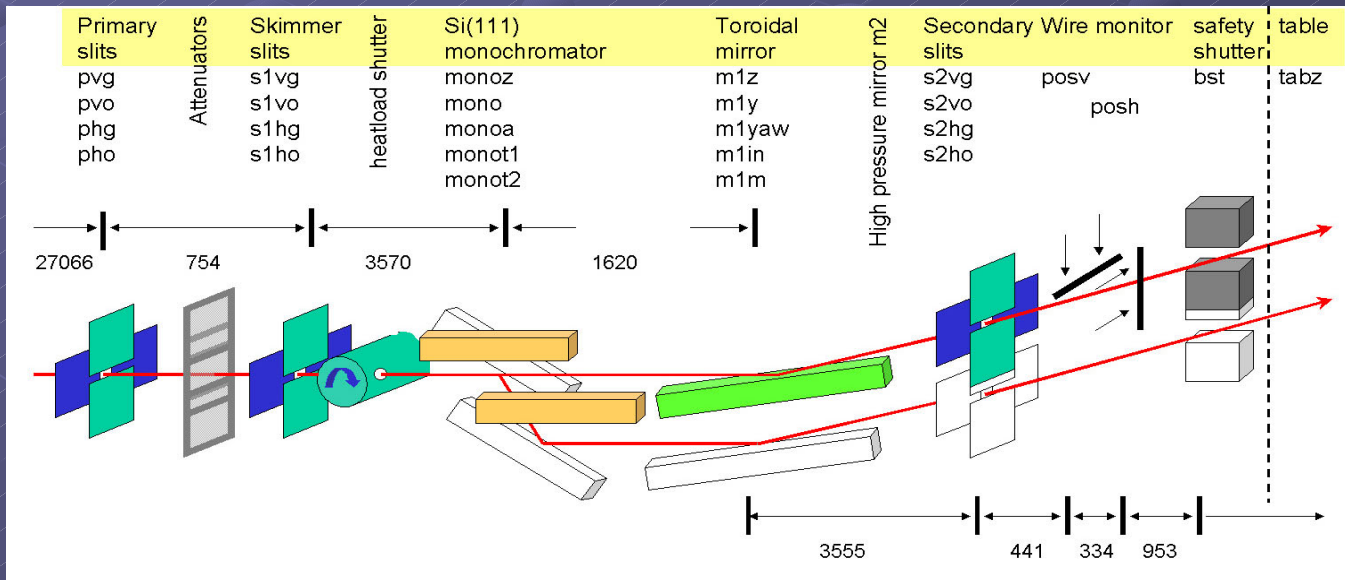
Equipment to measure Pb_3O_4 at high pressure



Selection of Diamond Anvil Cells

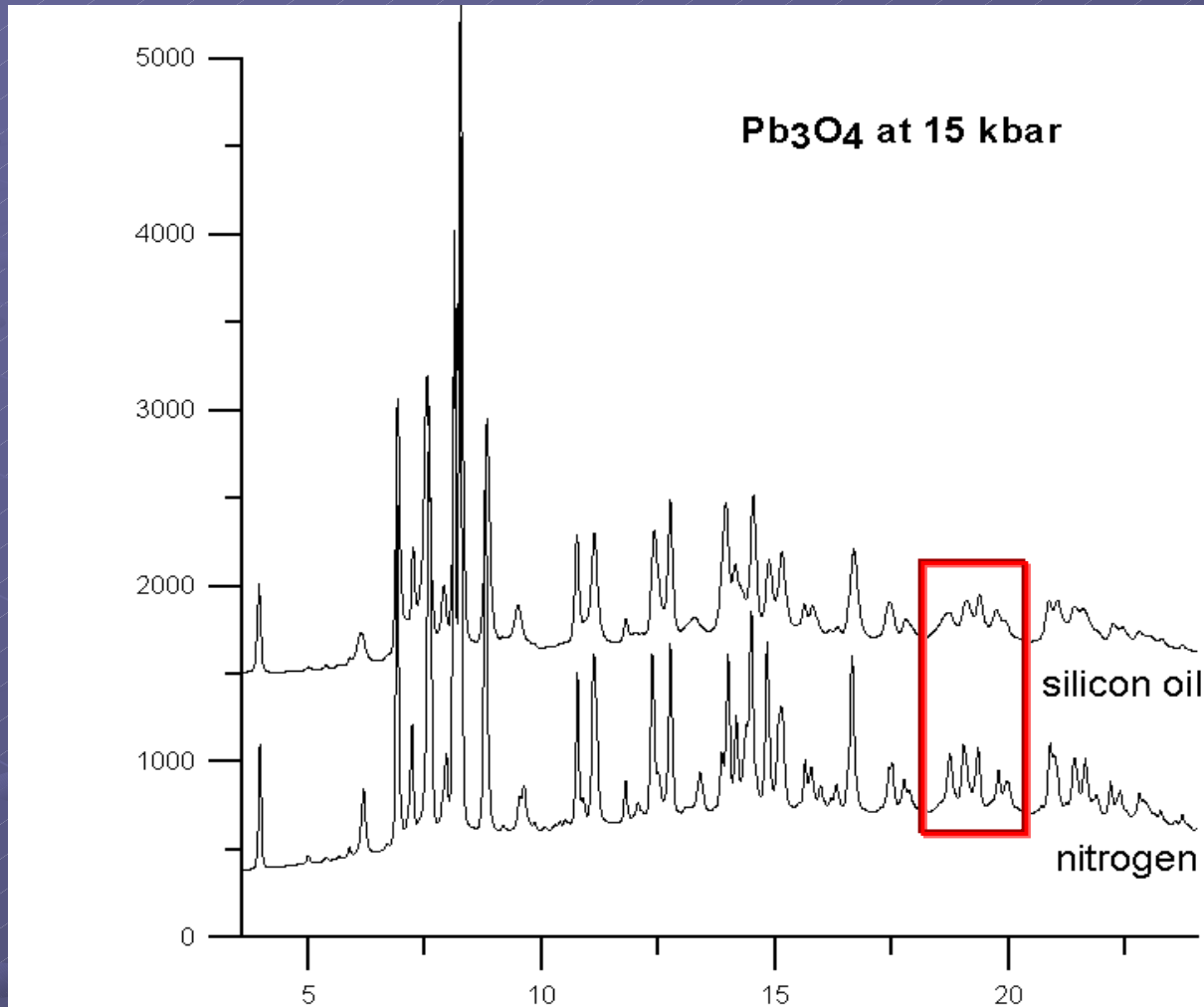


Mar345 image plate detector



Design of multi purpose optics hutch at ID9, ESRF, high pressure, time resolved (Laue)

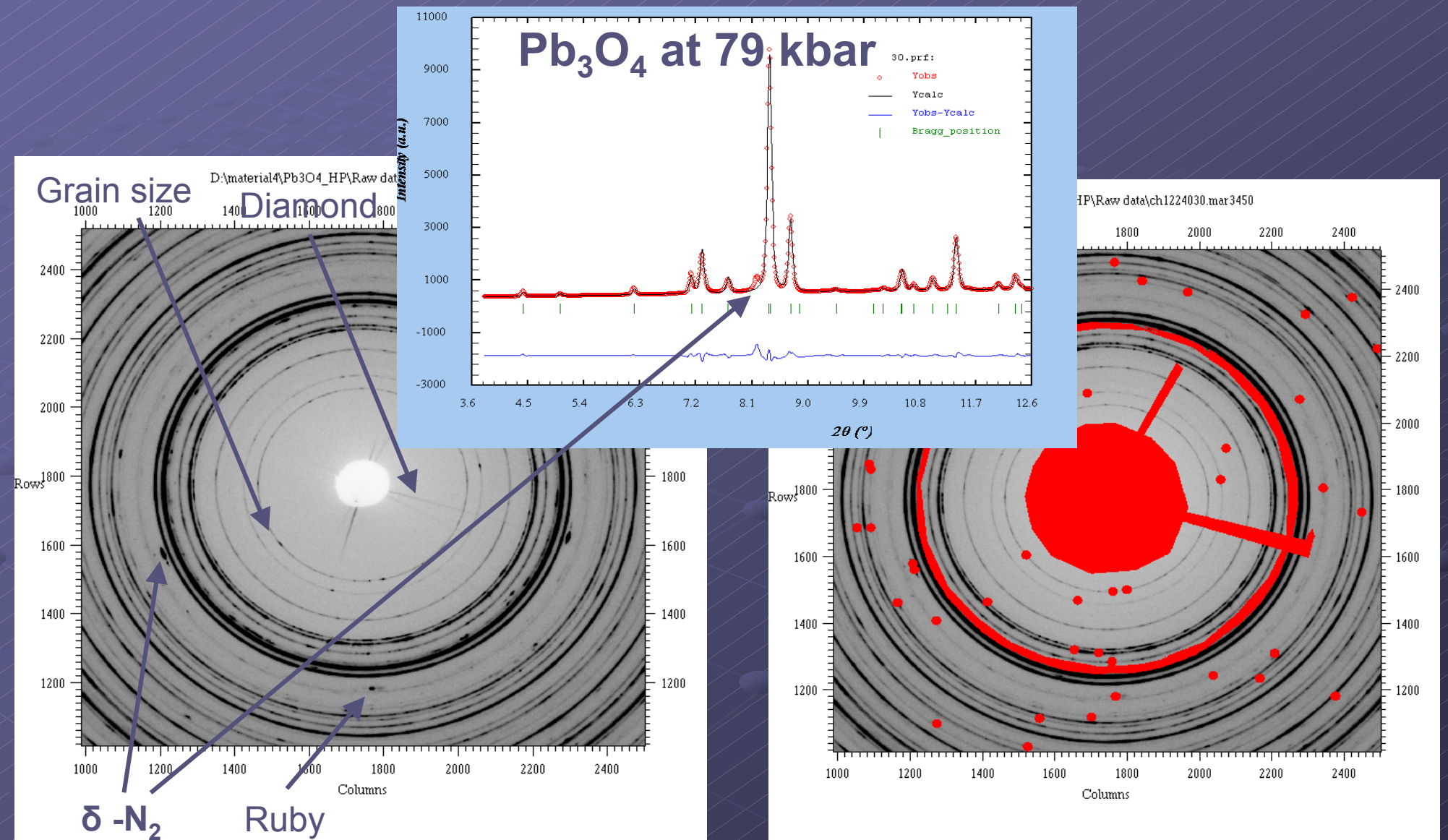
Influence of pressure medium on the diffraction peak width of Pb_3O_4



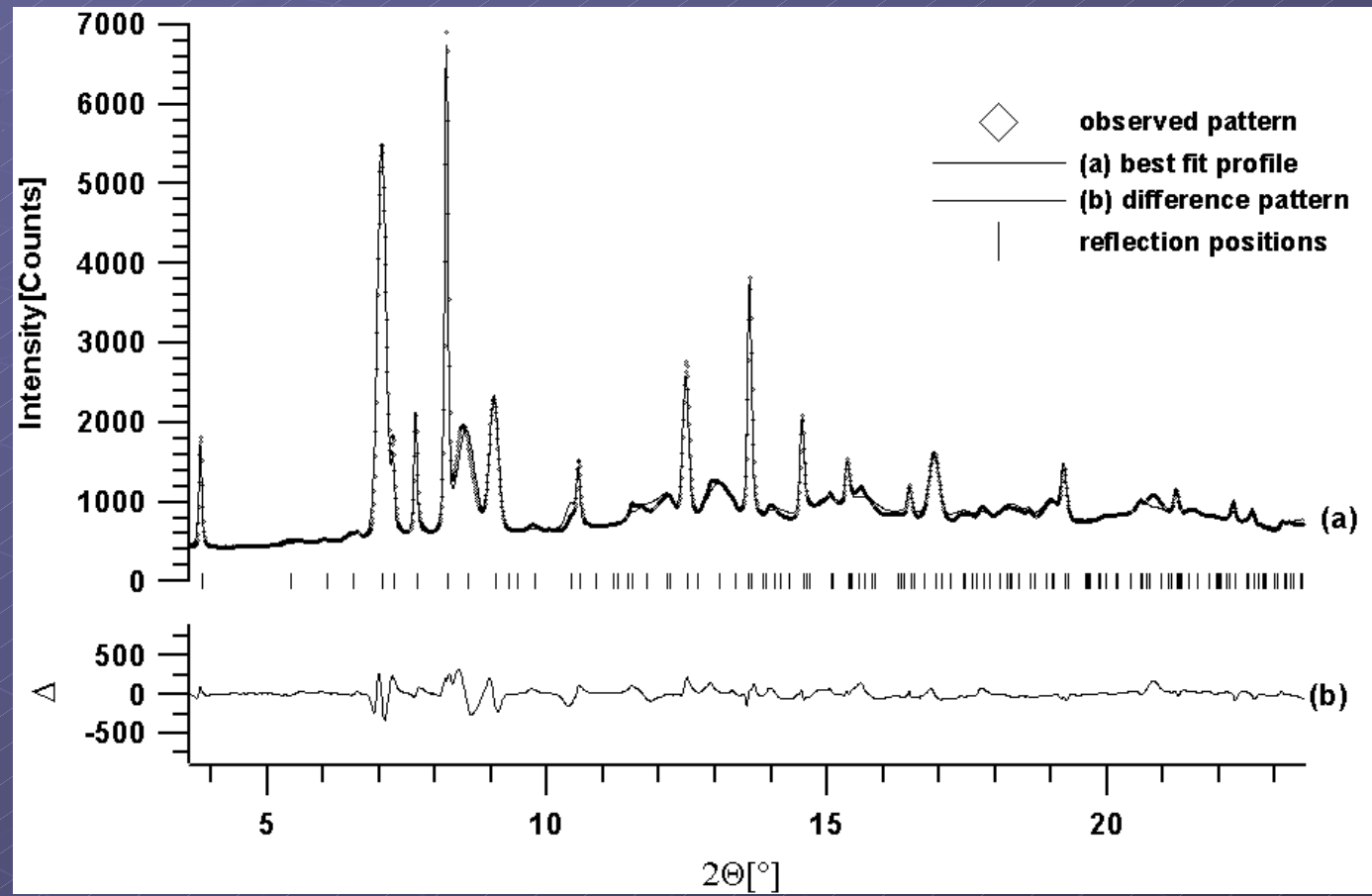
Cryogenic loading of DAC

Dependence of FWHM on pressure medium

Data reduction

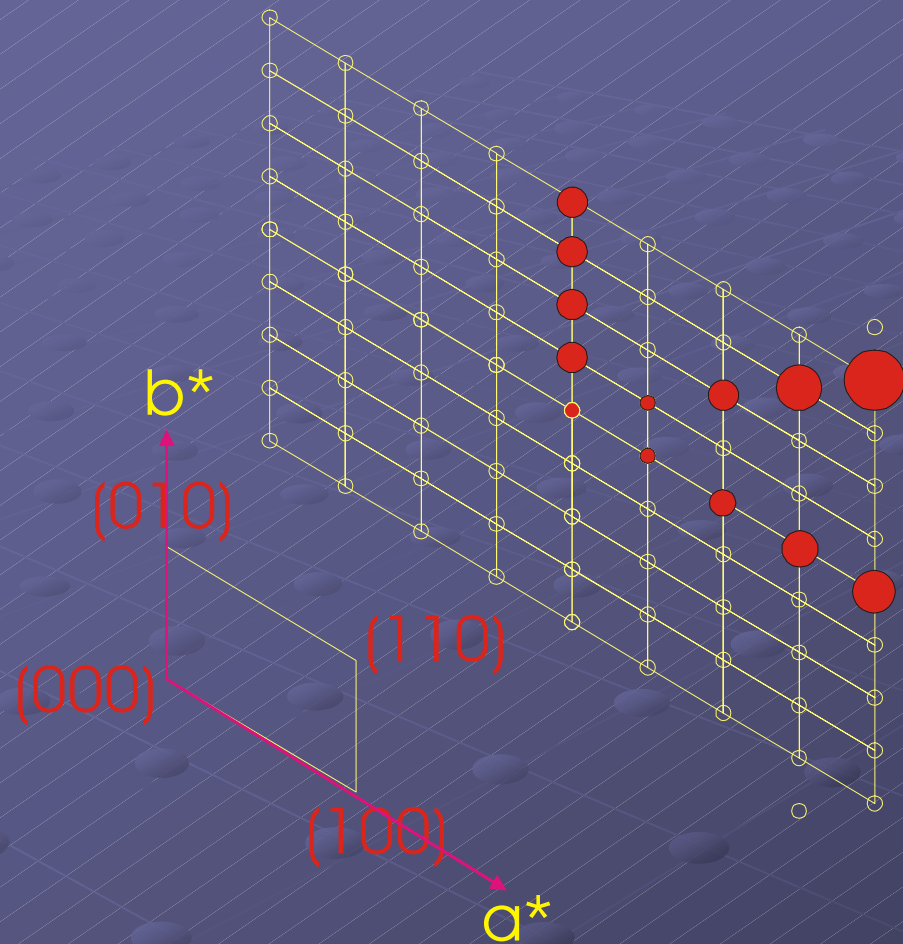


Anisotropic peak broadening in Pb_3O_4



Rietveld plot of the low pressure phase I of Pb_3O_4 at $P = 1.1 \text{ kbar}$ ($\lambda = 0.41594 \text{ \AA}$)

Anisotropic Microstrain:



The anisotropic microstrain distribution is directly related to the elastic constants of the material.

The peak width $\sim \tan\theta$ but proportionality constant is different in different directions of (hkl) .

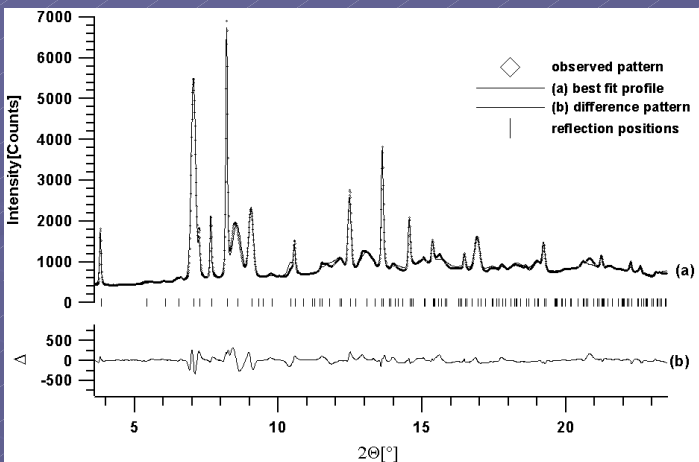
$$S^2 = S_{400}h^4 + S_{301}h^3l + \dots + S_{004}l^4$$

$$\delta d / d = \pi / 180 S d^2$$

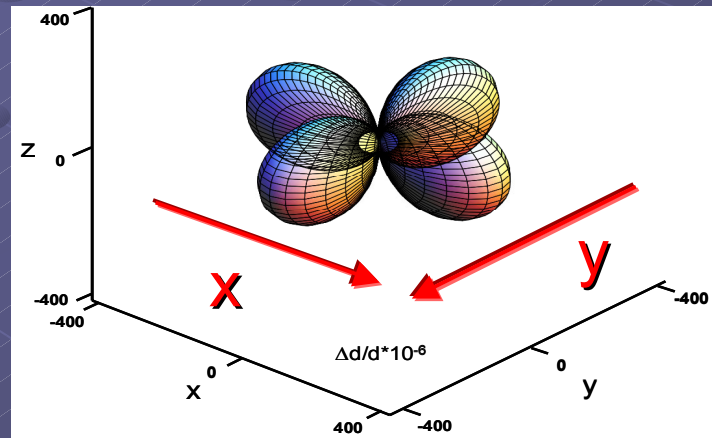
$$\text{FWHM in } 2\theta = (360 / \pi)(\delta d / d) \tan \theta.$$

The phenomenological model of P. W. Stephens, *J. Appl. Cryst.* **32**, 281-289, 1999 is used:

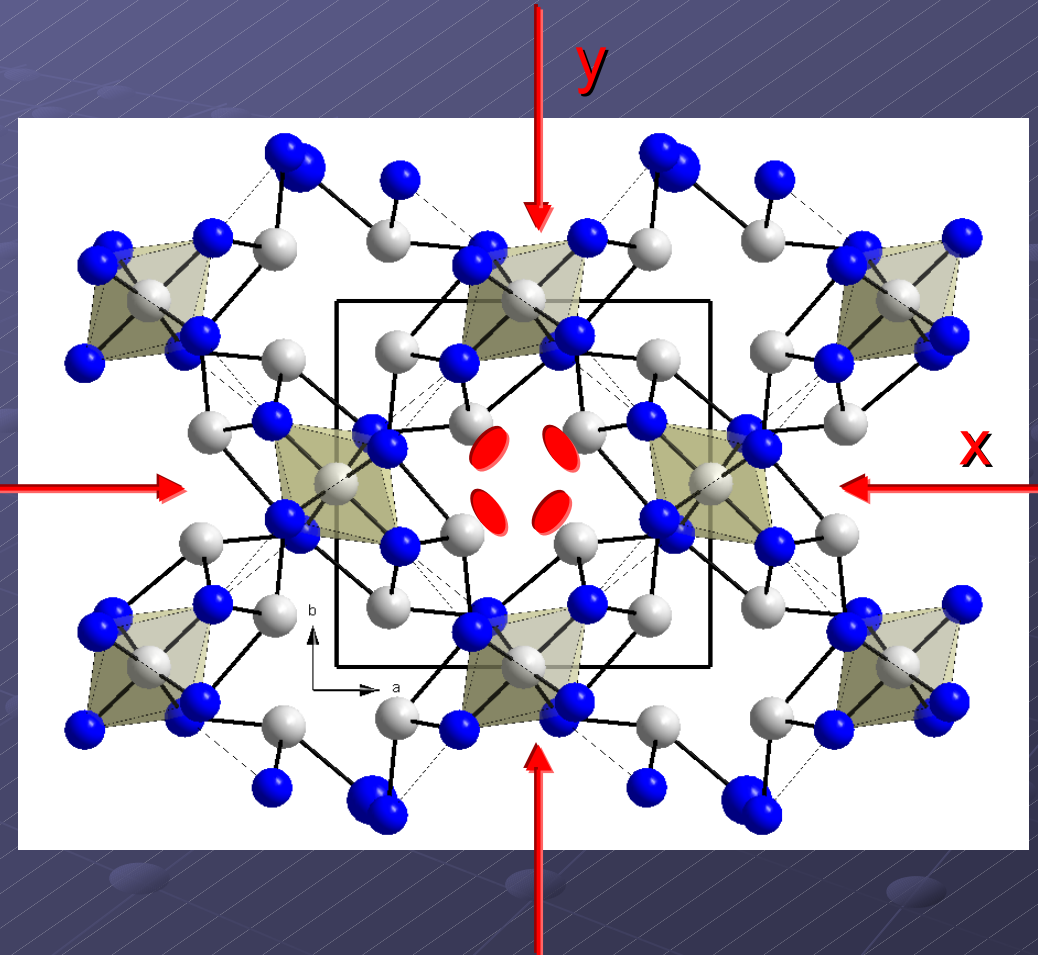
Microstrain in the tetragonal phase I of Pb_3O_4



Rietveld plot of phase I of Pb_3O_4
at $P = 1.1 \text{ kbar}$ ($\lambda = 0.41594 \text{ \AA}$)

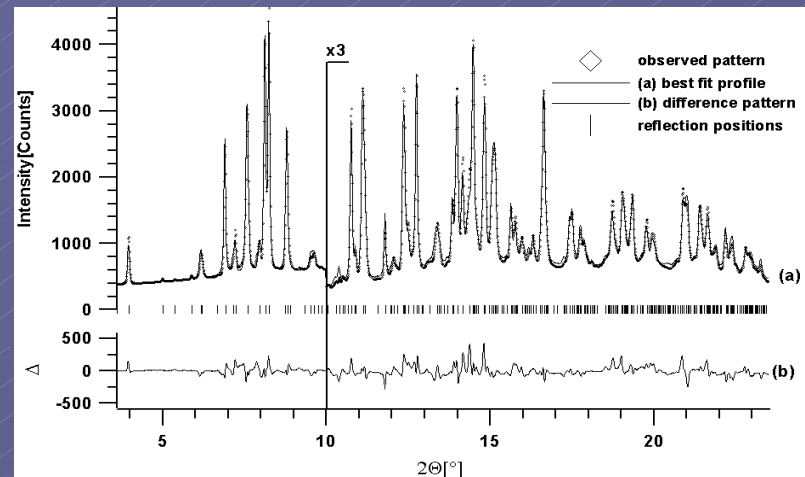


Isosurface of the anisotropic microstrain
of phase I of Pb_3O_4 at 0.6 kbar

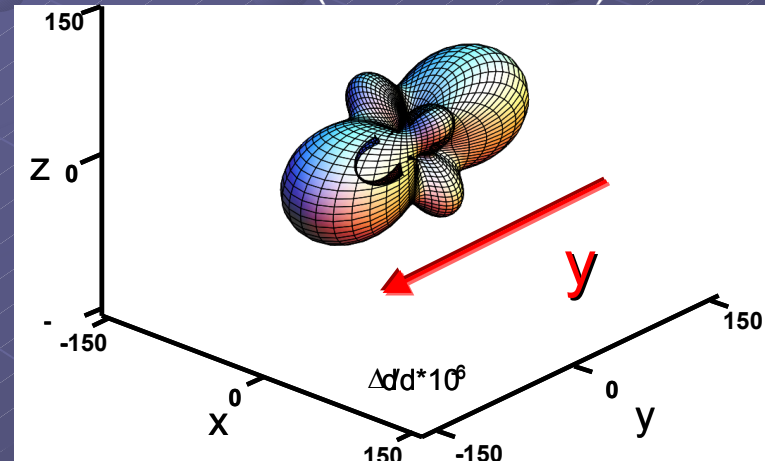


Pb_3O_4 (Pb^{+IV}Pb^{+II}O₄) at ambient conditions

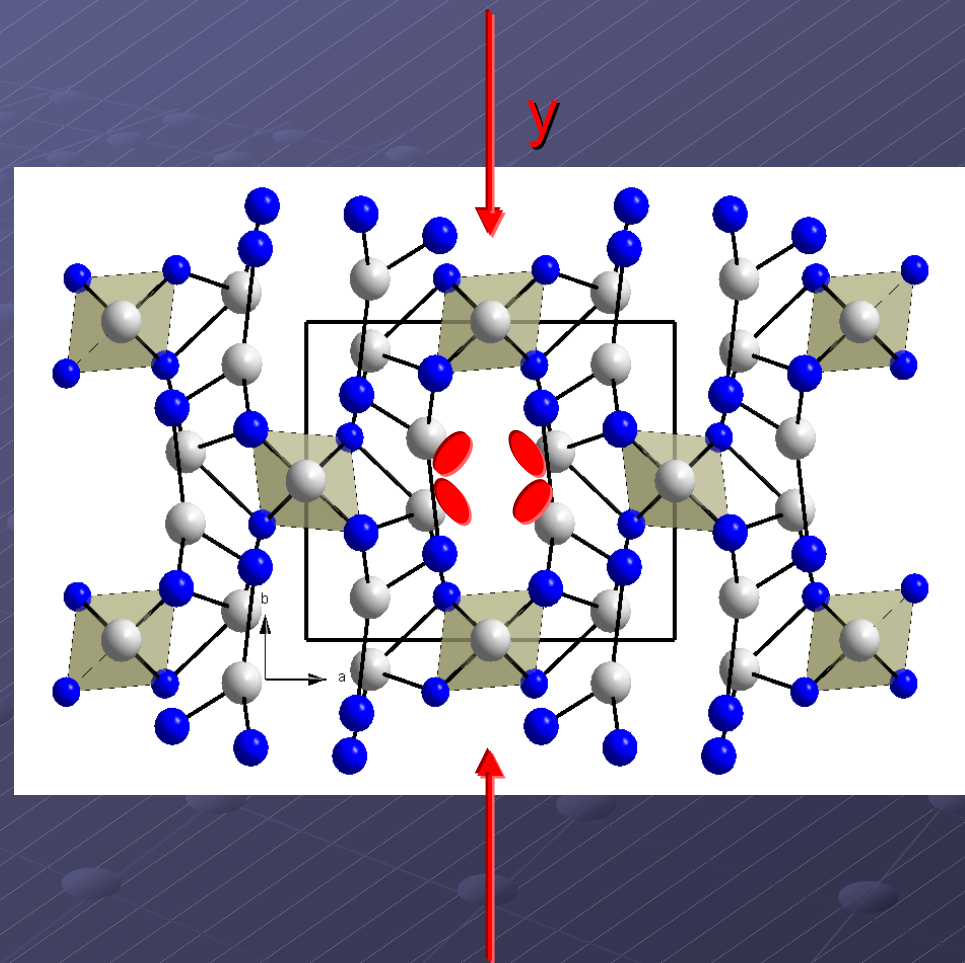
Microstrain in the orthorhombic phase II of Pb_3O_4



Rietveld plot of phase II of Pb_3O_4
at $P = 15 \text{ kbar}$ ($\lambda = 0.41594 \text{ \AA}$)

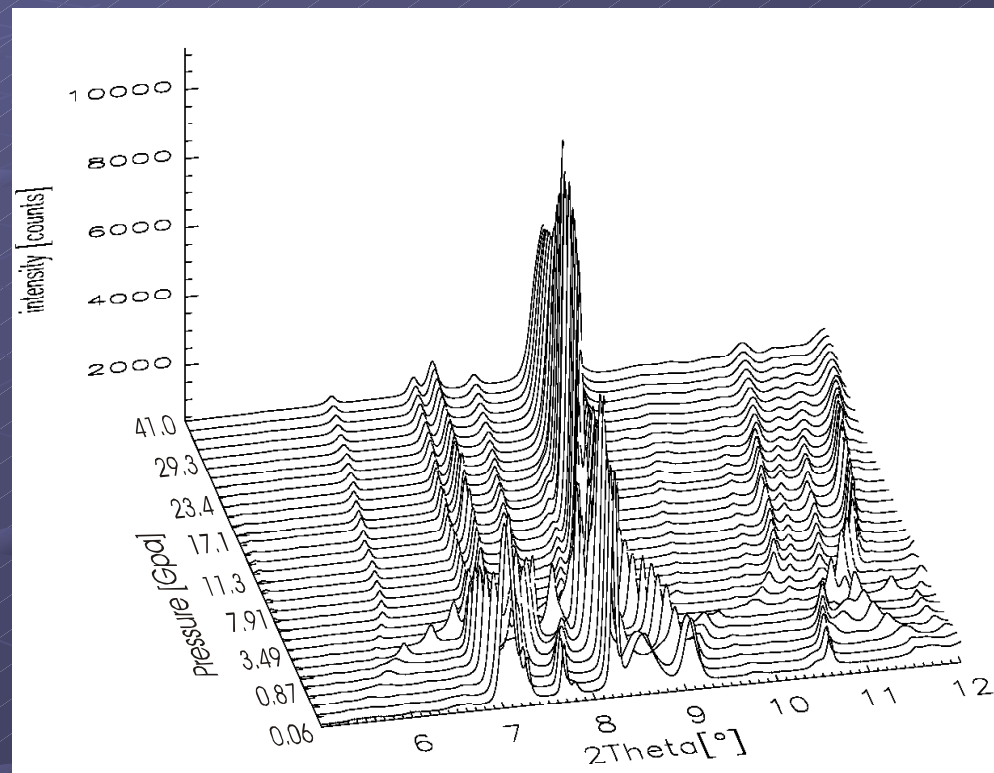
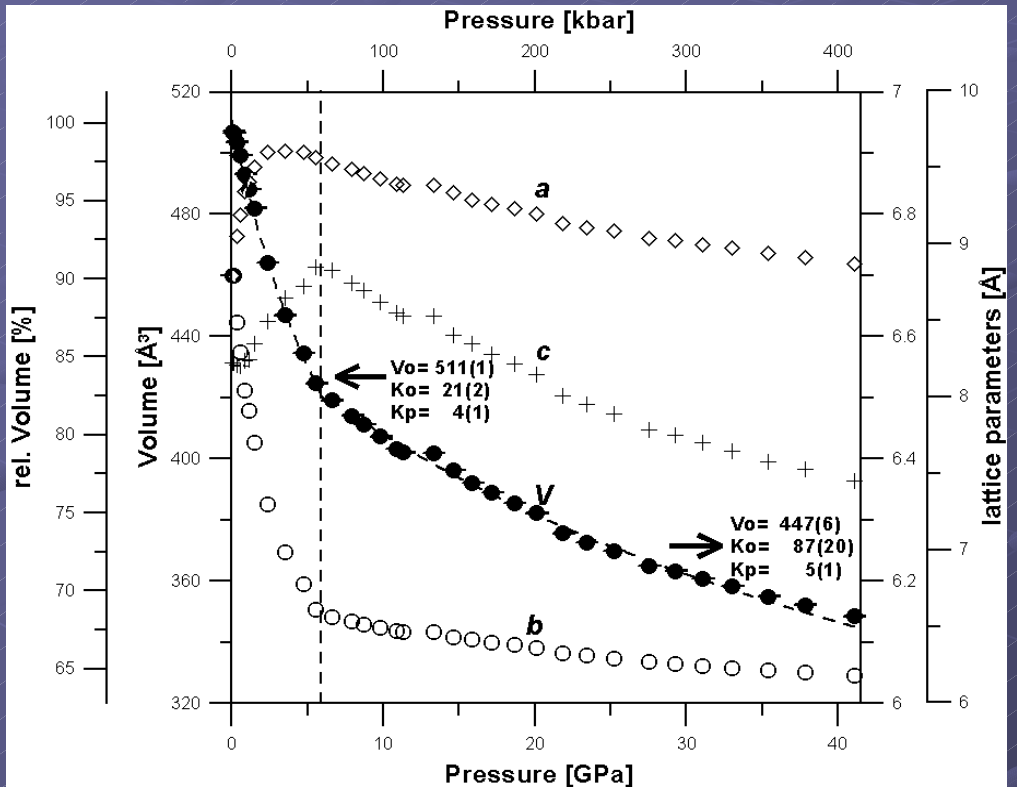


Isosurface of the anisotropic microstrain
of phase II of Pb_3O_4 at 34 kbar



$\text{Pb}_3\text{O}_4 (\text{Pb}^{+IV}\text{Pb}^{+II}_2\text{O}_4)$ at 34 kbar

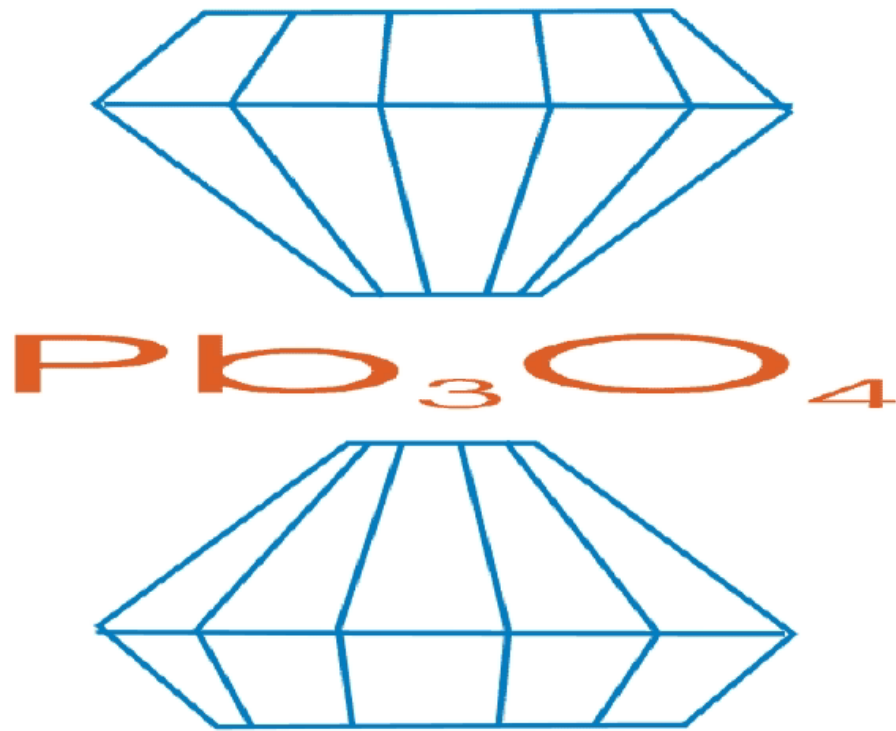
Pb_3O_4 at high pressure



Effect of pressure on the crystal structure of minium (pressure range: 0-420 kbar)
Left: Lattice parameters, (rel.) volume and bulk moduli
Right: Powder diffraction patterns

Pb_3O_4 between 0 and 410 kbar

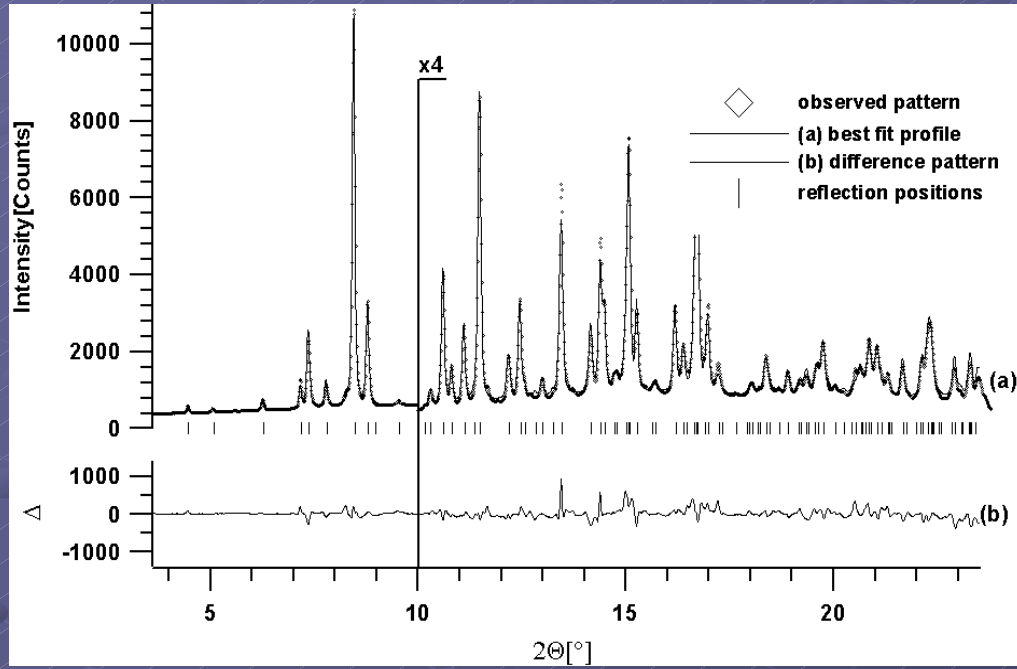
Phase transitions of Pb_3O_4 at high pressure
up to 41 Gpa



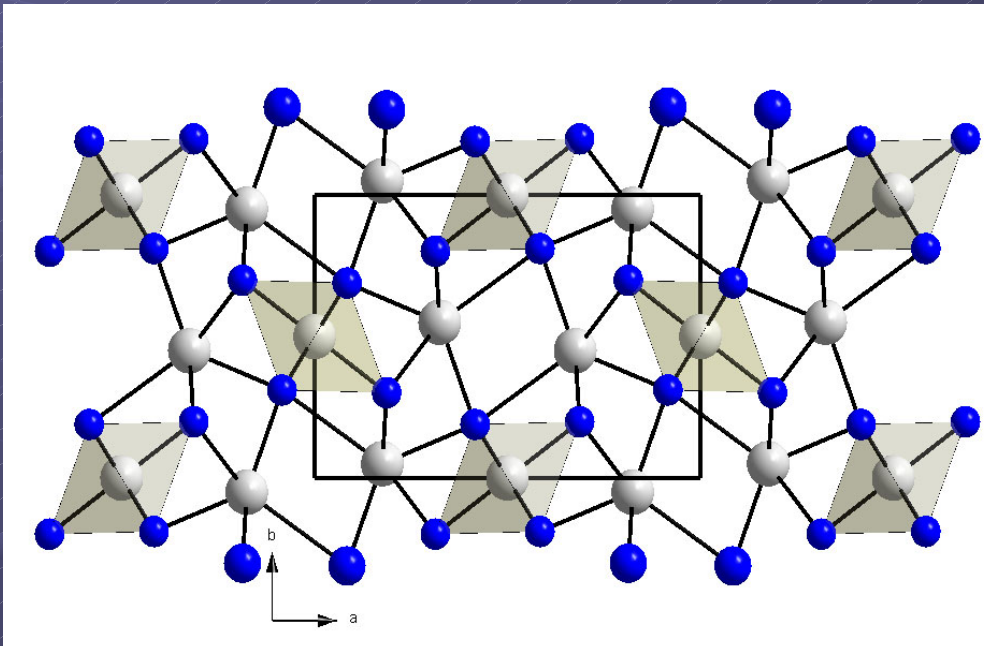
R. E. Dinnebier, S. Carlson & M. Jansen

2002

The high pressure phase III of Pb_3O_4 at 133 kbar



Rietveld plot of Pb_3O_4 at 133 kbar



Ball and stick model of the crystal structures of Pb_3O_4 at 133 kbar (phase III) in a projection along c-axis. The Pb^{+4}O_6 octahedra are shown.

Comparison to isotropic crystal structures

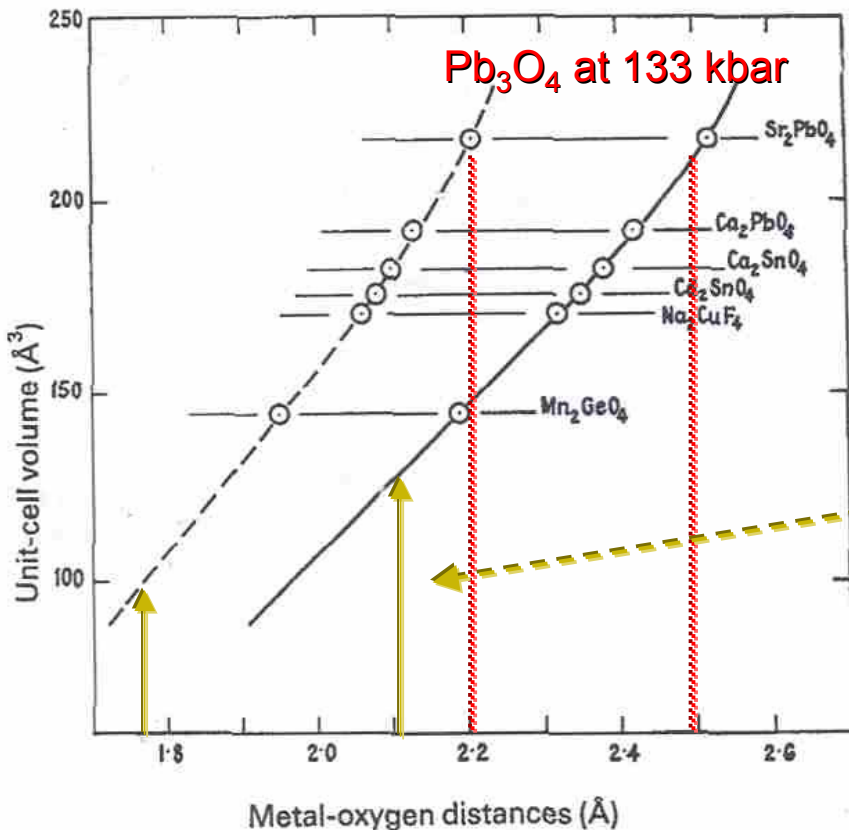
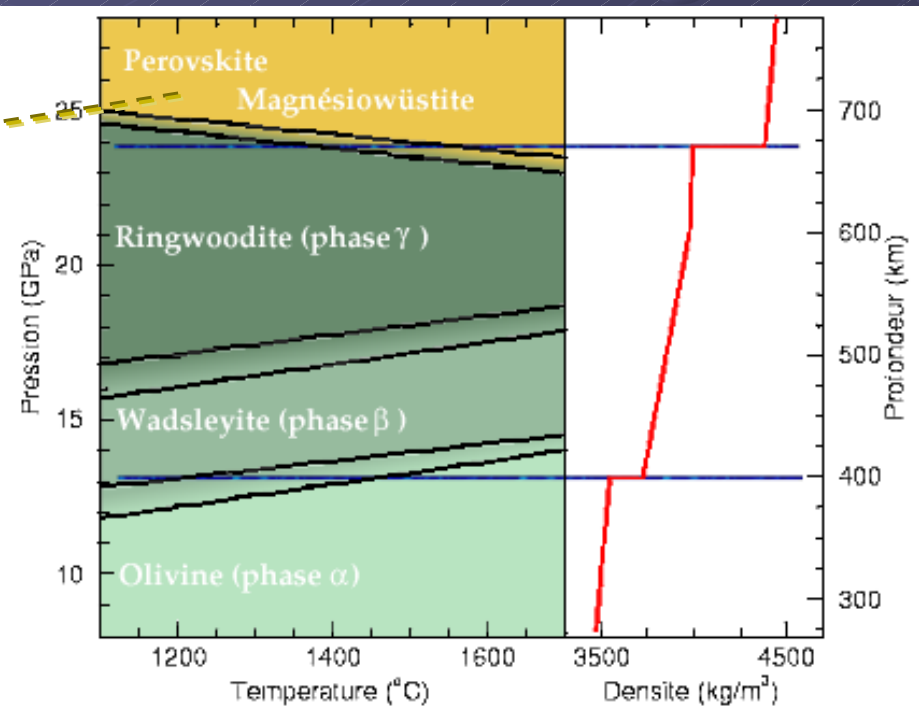
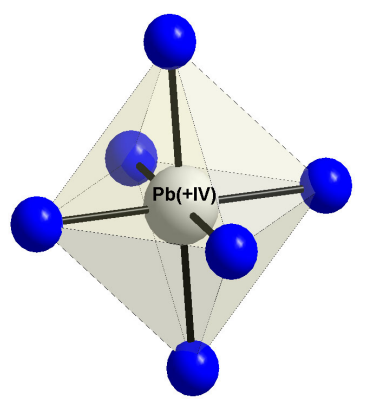


Fig. 3. Volume of unit cell *versus* the average octahedral (dashed line) and trigonal prismatic (full line) bond distances in Mn_2GeO_4 and isomorphous compounds. Verticals drawn from 1.77 \AA (average Si-O bond length) and 2.10 \AA (average Mg-O length), $\pm 0.05 \text{\AA}$, should intersect the dashed and full lines at the same unit-cell volume if Mg_2SiO_4 is to form the Mn_2GeO_4 structure.

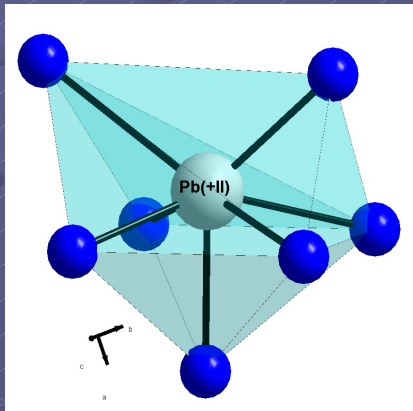
Phase III of Pb_3O_4 is Isotypic to the high pressure form of Mn_2GeO_4 , a member of the olivine group
(Wadsley, Reid & Ringwood, 1968,
Acta Cryst. B 24, 740-742)



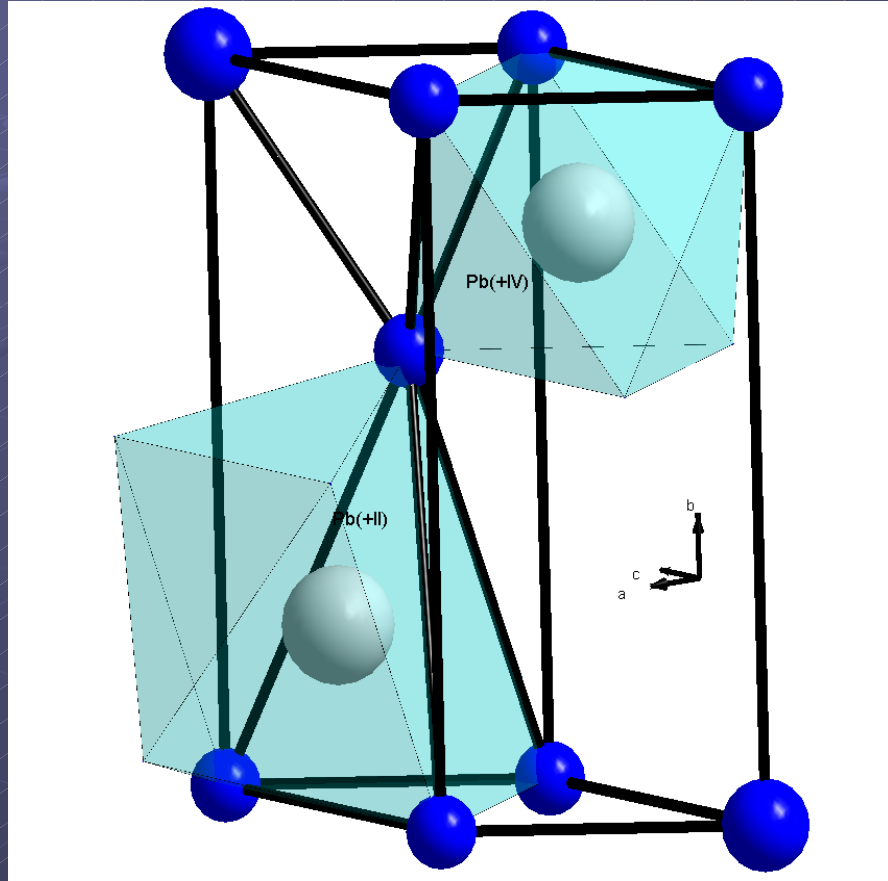
Coordination polyhedra in the high pressure phase III of Pb_3O_4



Regular Pb^{+4}O_6 octahedron (left) in Pb_3O_4 at 13.3 GPa (phase III)

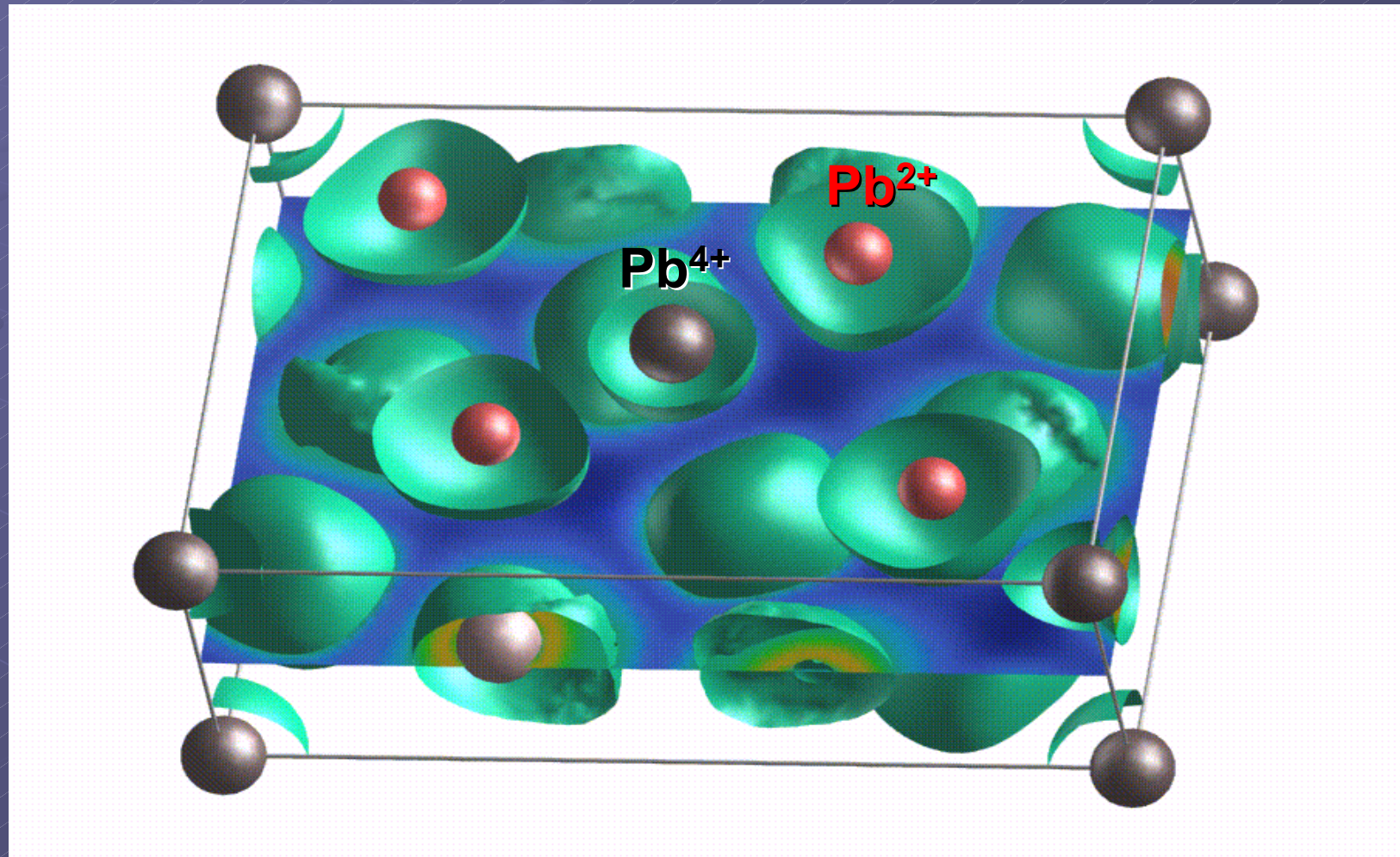


Irregular capped trigonal prisms.
Left: $\text{Pb}^{+2}\text{O}_{6+1}$ in Pb_3O_4 at 13.3 GPa (phase III)
Right: $\text{Sr}^{+2}\text{O}_{6+1}$ in Sr_3PbO_4 at ambient conditions



Hexagonal closed packing (hcp) arrangement of Pb_3O_4 at 13.3 GPa leading to the formula $(\text{Pb}^{+4}\square_3)^{\text{VI}}(\text{Pb}^{+2}\square_6)^{\text{IV}}\text{O}_4$.

ELF calculation for the high pressure phase III of Pb_3O_4 at 133 kbar

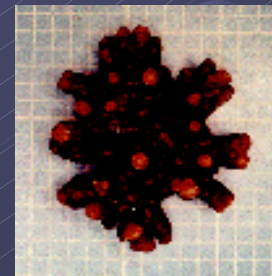
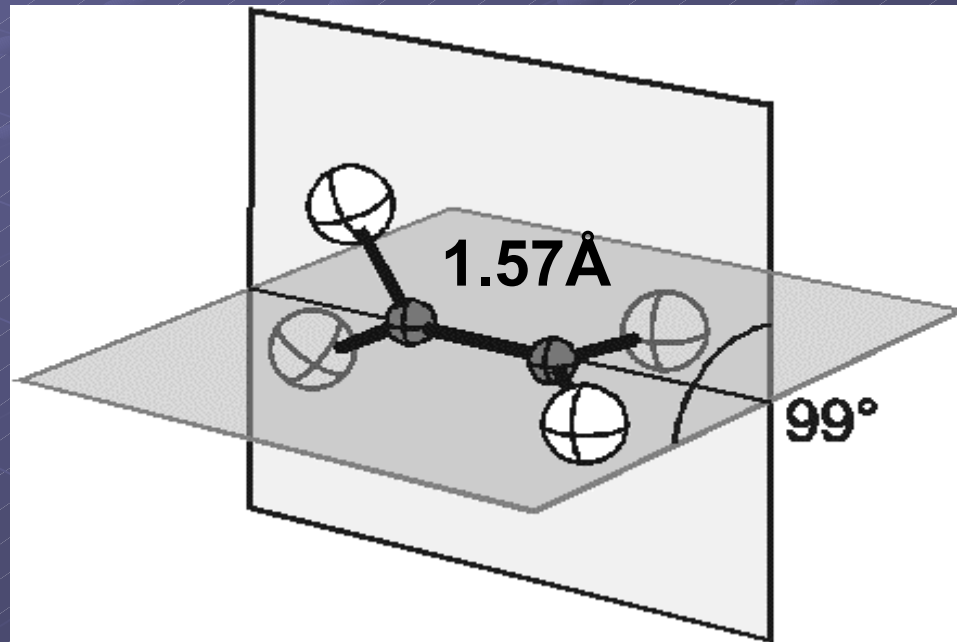
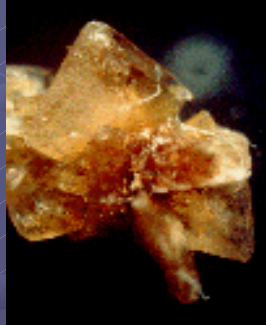


Isosurface of the electron localization function (ELF=0.385)

Crystal and Molecular Structures of Alkali Oxalates

First Proof of a twisted Oxalate Molecule in the Solid State

Robert E. Dinnebier, Sascha Vensky, Martin Panthöfer & Martin Jansen
2002, J. Inorg. Chem., in press



The oxalate dianion $\text{C}_2\text{O}_4^{2-}$

Global optimization methods in direct space:

The method of simulated annealing for structure determination from powder diffraction data

Selection of T and δ according to
an annealing protocol

Setting an initial atom configuration $\{X\}$

Calculation of χ^2 (intensity or profile)

e.g.
$$\chi^2 = \sum_h \sum_k (I_h - c|F_h|^2)(V^{-1})_{hk} (I_k - c|F_k|^2)$$

Random change in atom configuration

$\{X\}_{\text{new}} = \{X\} + \delta\{X\}$
(translation, rotation, torsion, occupancy...)

Calculation of new χ^2_{new}
and $\Delta\chi^2 = \chi^2_{\text{new}} - \chi^2$

$\Delta\chi^2 > 0$

no

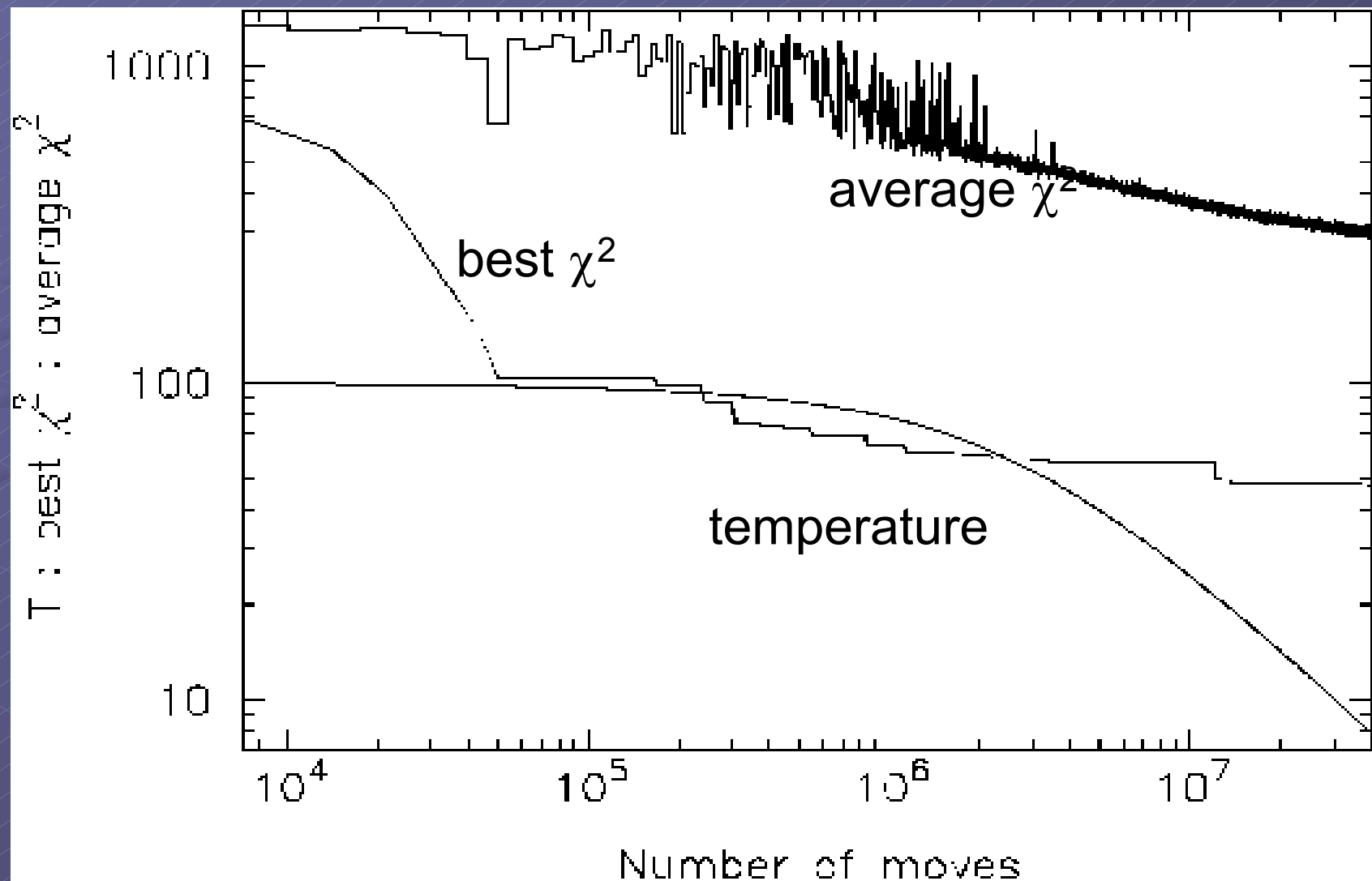
$\{X\} = \{X\}_{\text{new}}$

yes

$\{X\} = \{X\}_{\text{new}}$ with probability

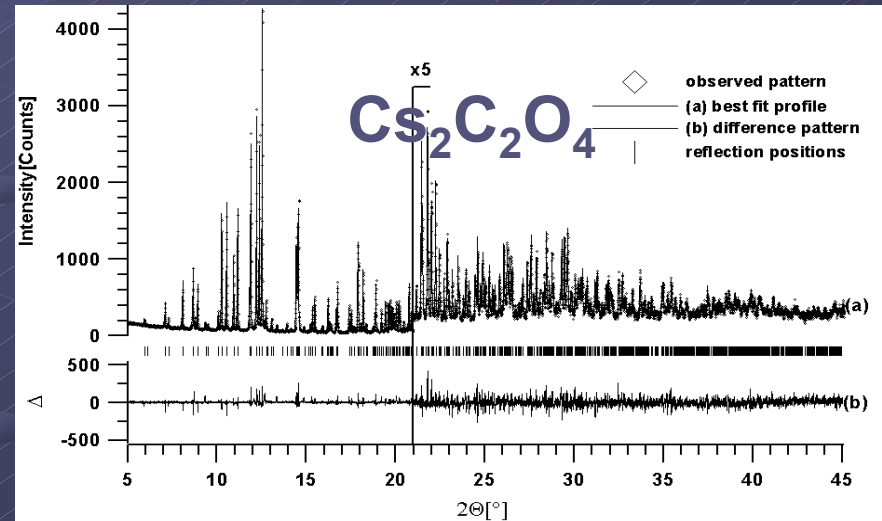
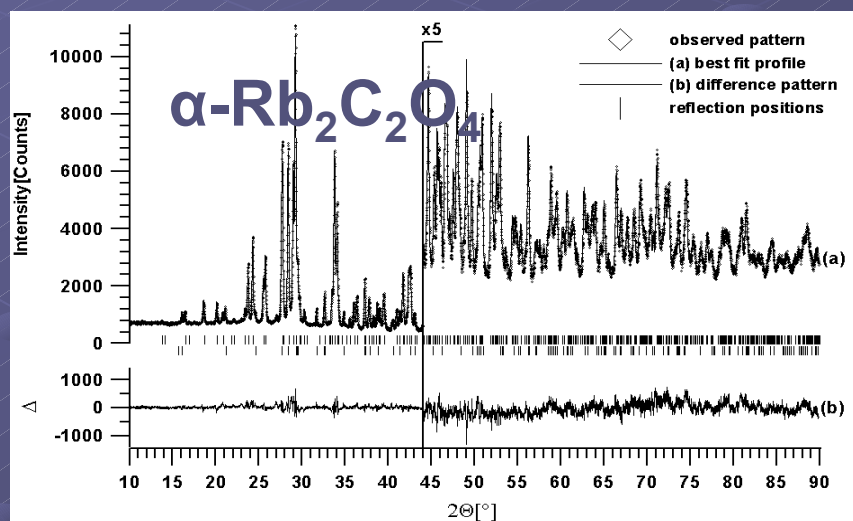
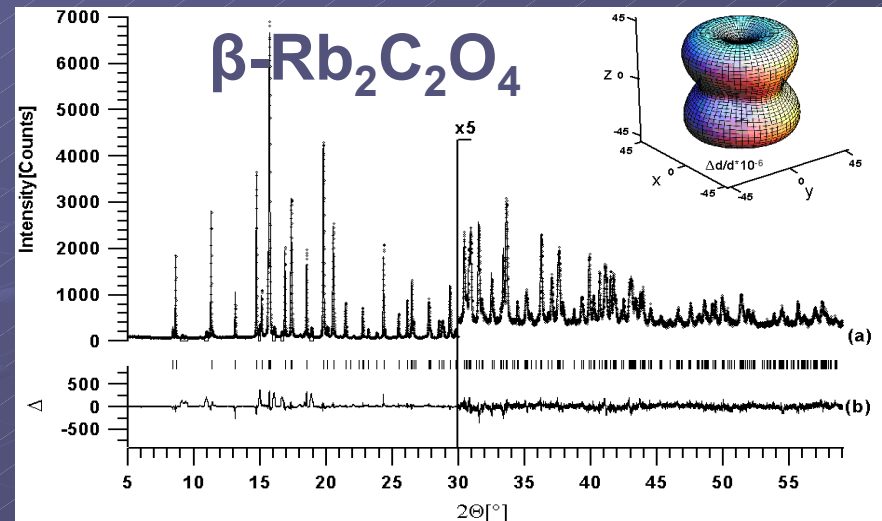
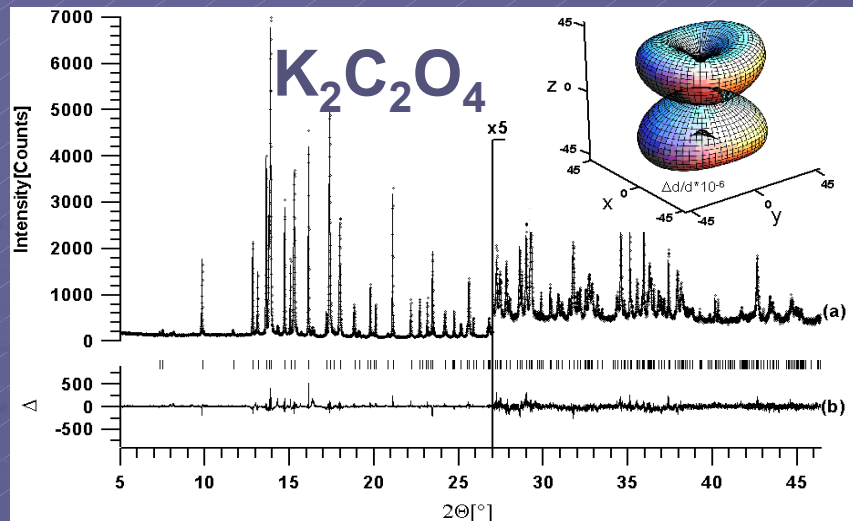
$$P = \exp\left(\frac{-\Delta\chi^2}{kT}\right)$$

‘Simulated annealing schedule’



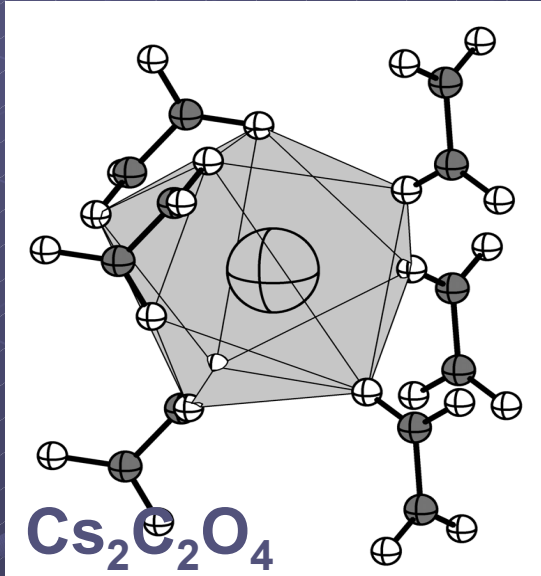
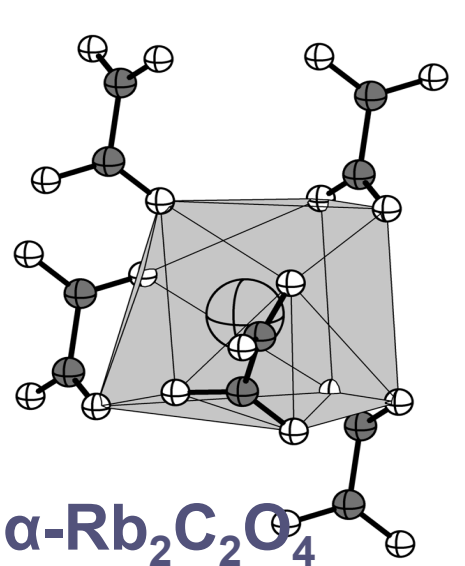
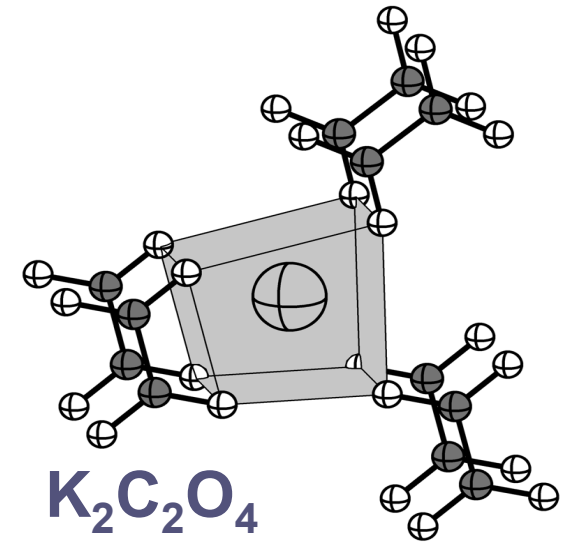
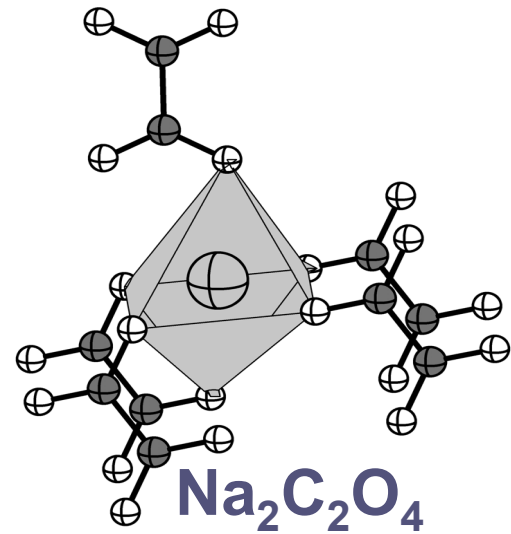
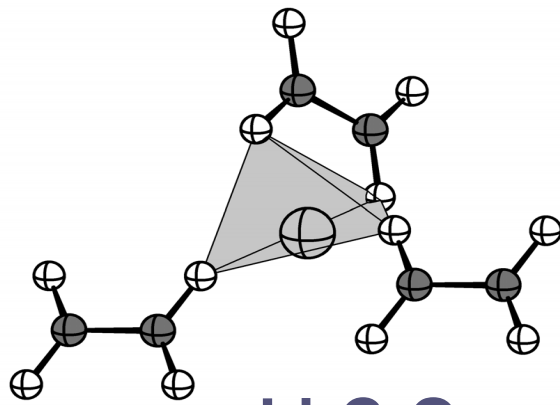
Chi² and temperature in dependence of the number of moves during simulated annealing run

Crystal and Molecular Structures of Alkali Oxalates

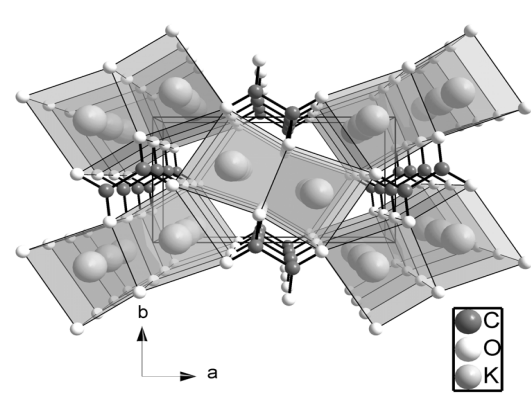


Powder pattern of $K_2C_2O_4$, $\beta-Rb_2C_2O_4$, $\alpha-Rb_2C_2O_4$, and $Cs_2C_2O_4$ (X3B1, NSLS).
The isosurface of anisotropic microstrain for $K_2C_2O_4$, $\beta-Rb_2C_2O_4$ is given

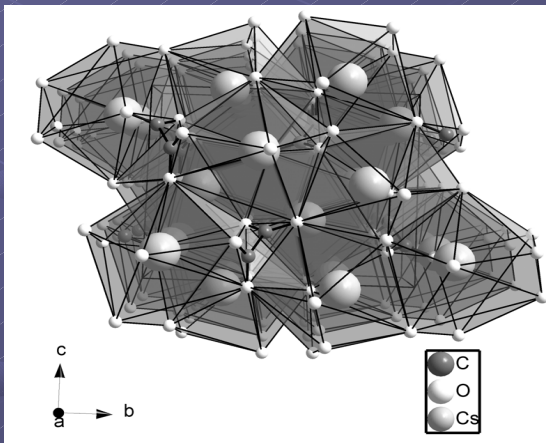
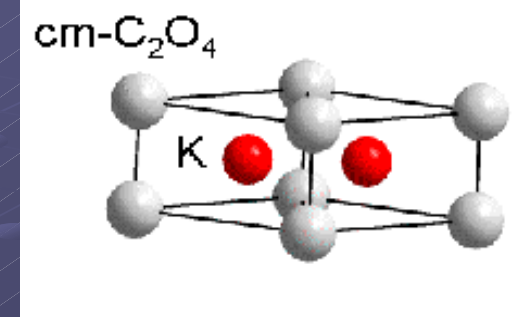
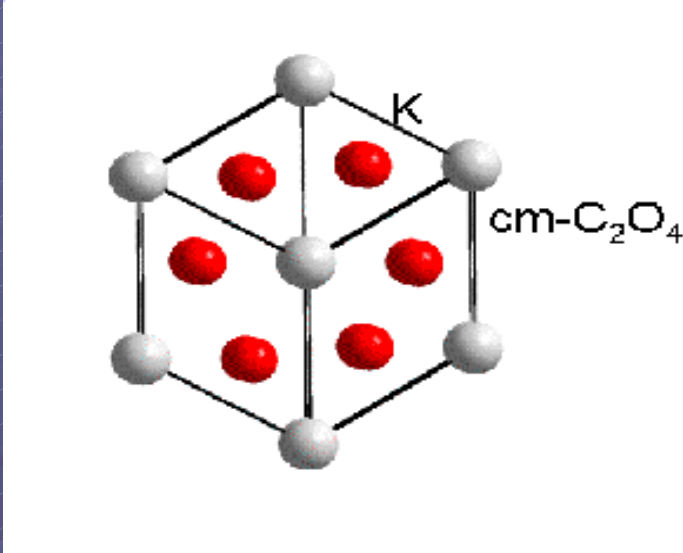
Crystal and Molecular Structures of Alkali Oxalates



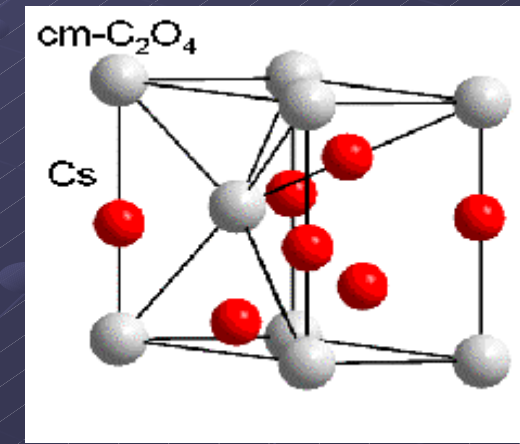
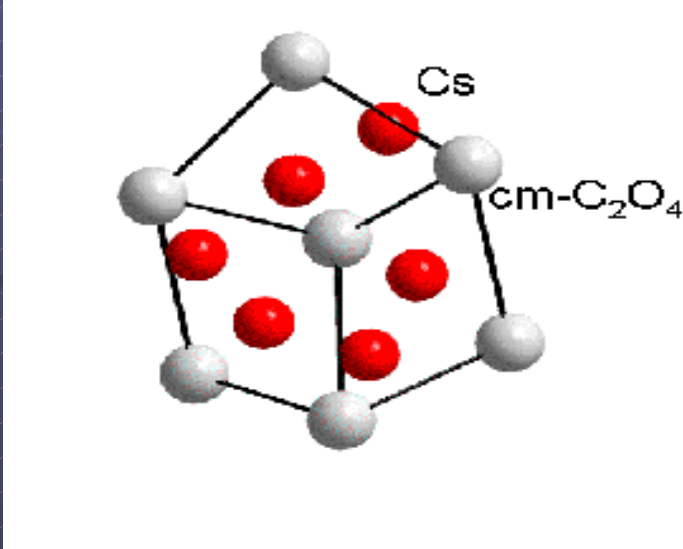
Crystal and Molecular Structures of Alkali Oxalates



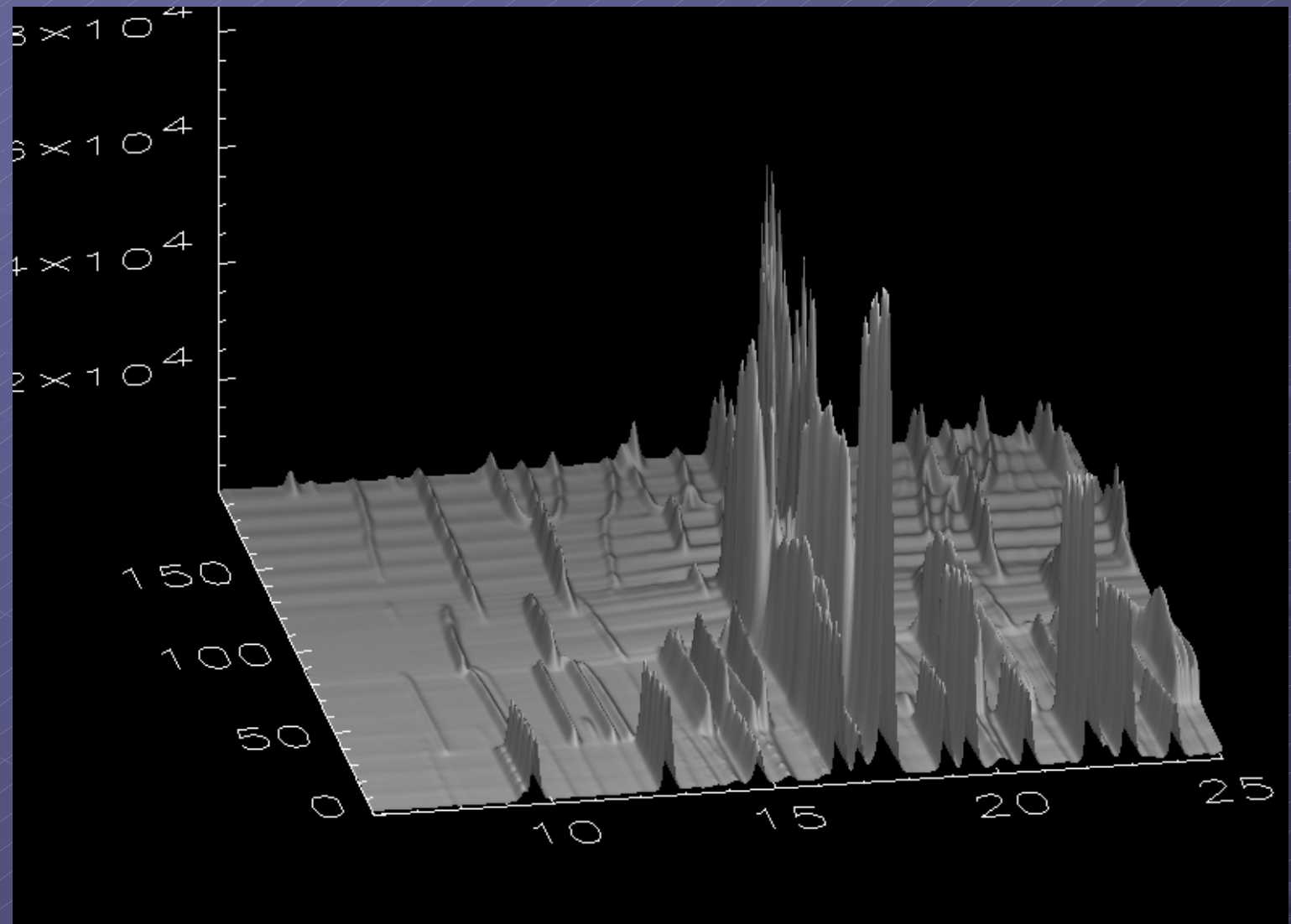
$\text{K}_2\text{C}_2\text{O}_4$



$\text{Cs}_2\text{C}_2\text{O}_4$



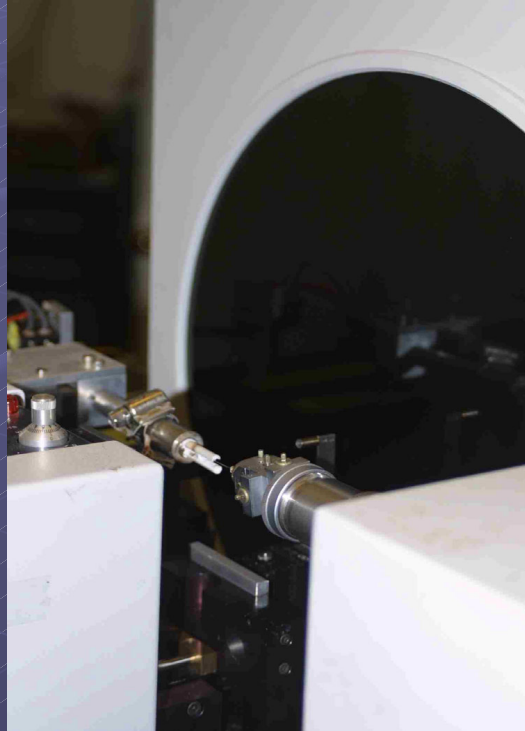
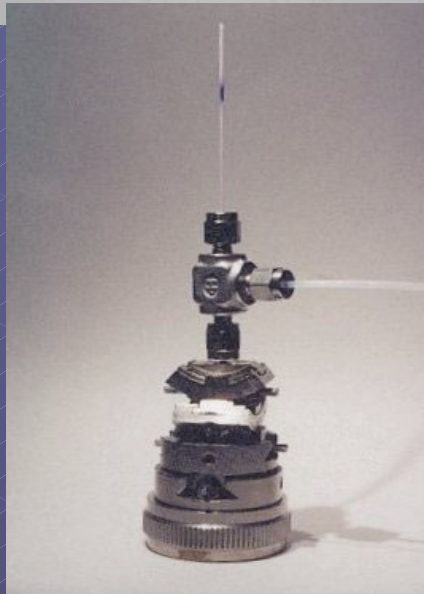
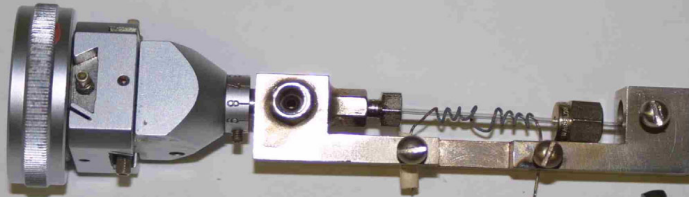
Thermal behavior of rubidium oxalate



Powder pattern of rubidium oxalate recorded at X7B (NSLS) in dependence on temperature ($25 \rightarrow 450 \rightarrow 75^\circ\text{C}$)

New developments for '*in situ*' powder diffraction

Equipment at beamline X7B, NSLS



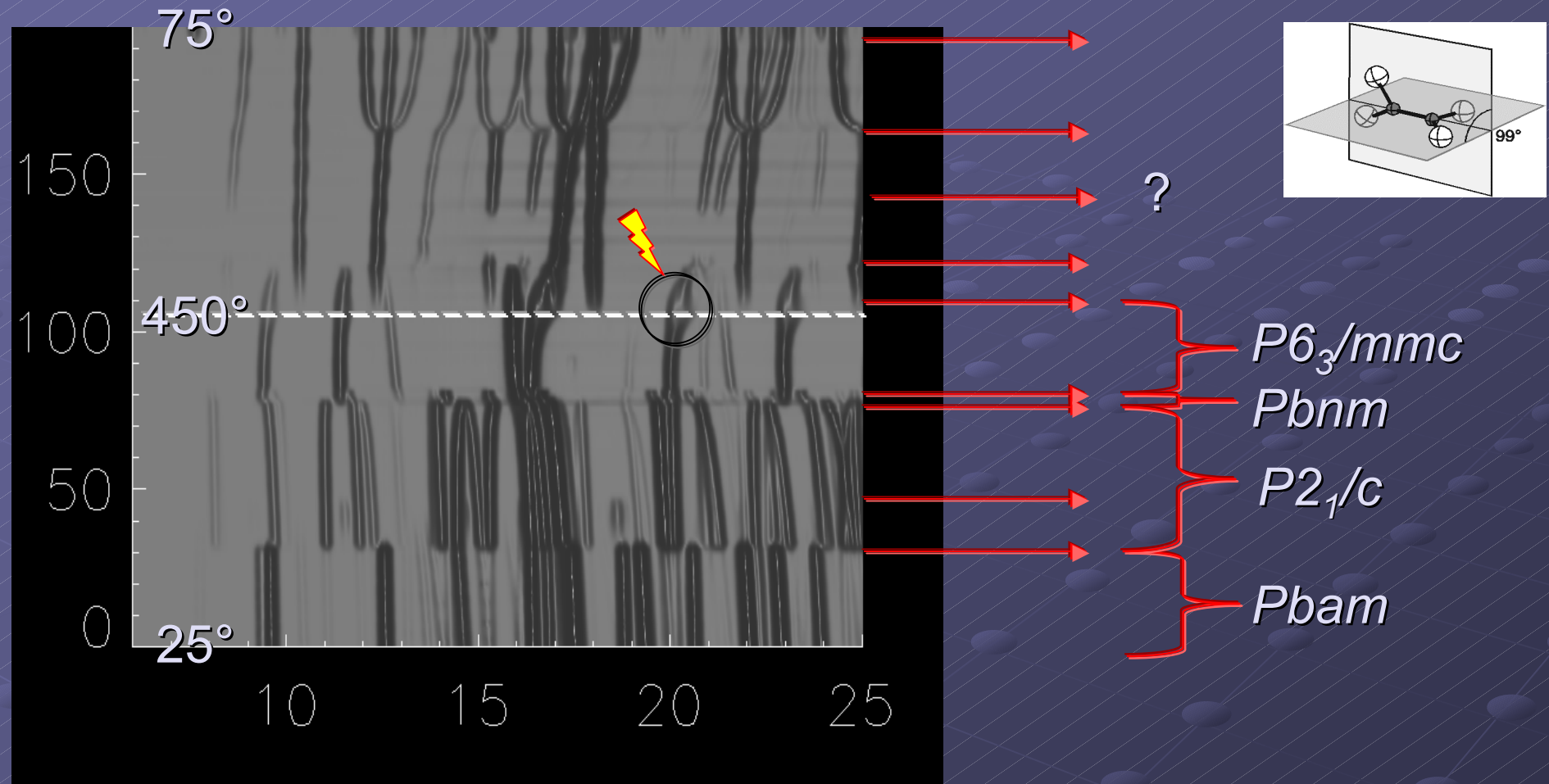
Mar345



Micro reactors with/without heater

Mass-spectrometer

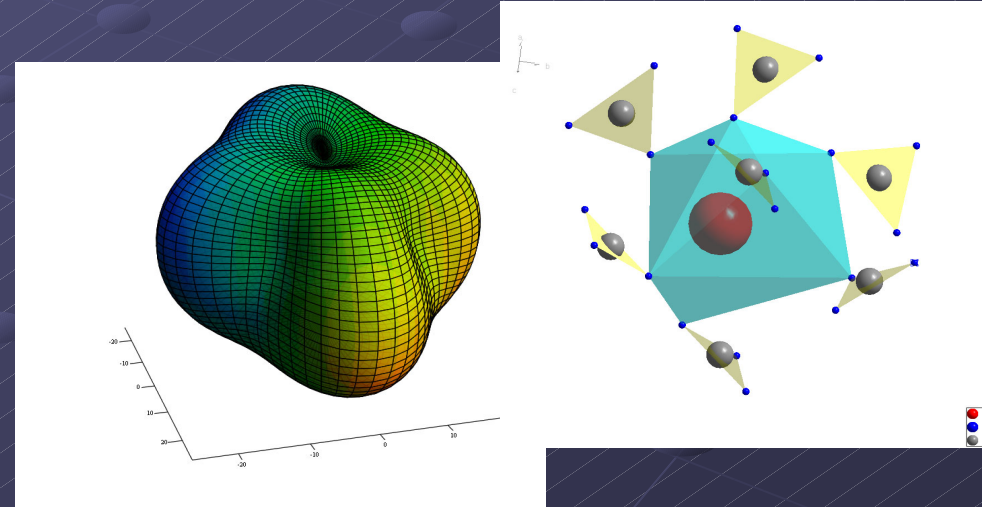
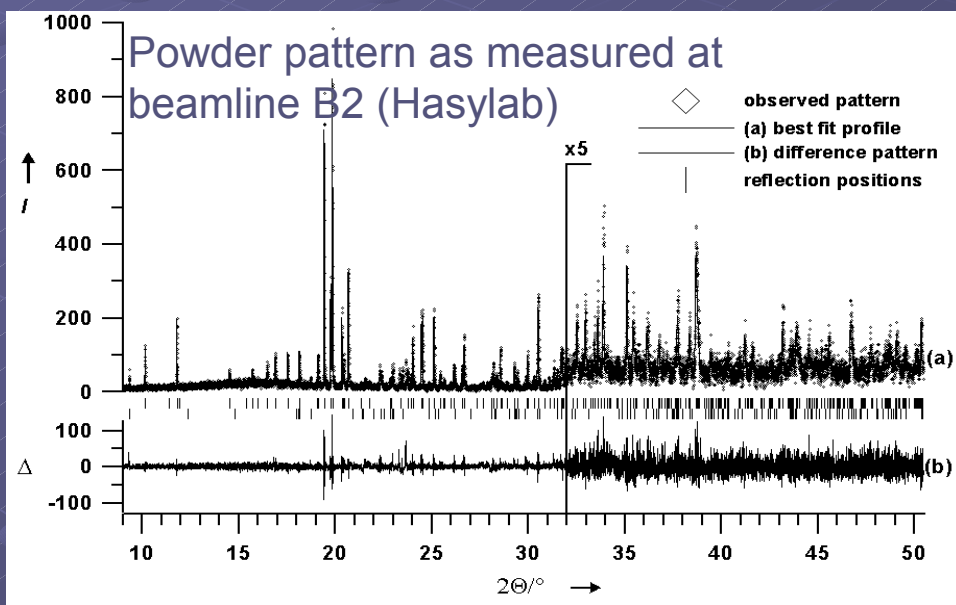
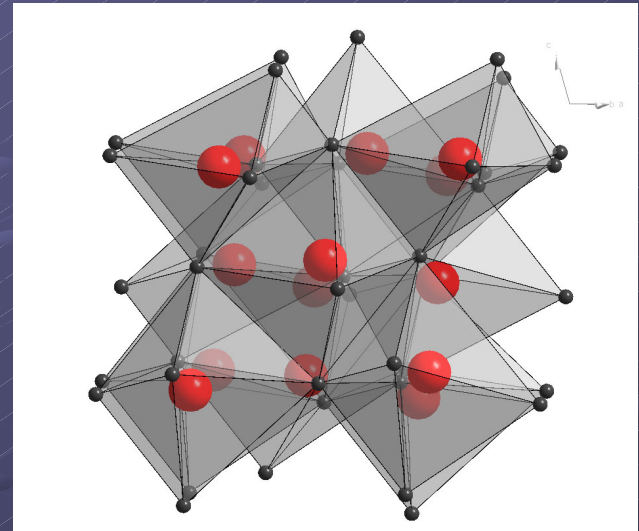
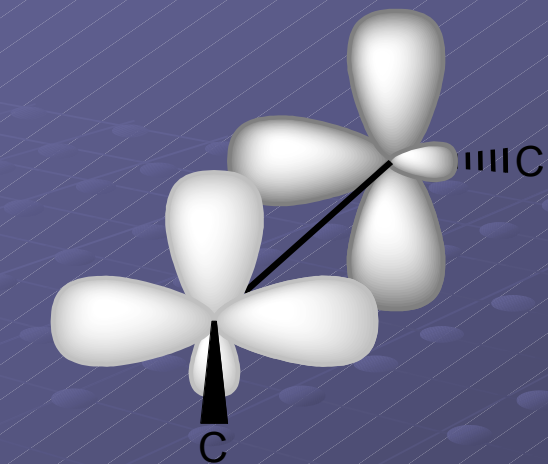
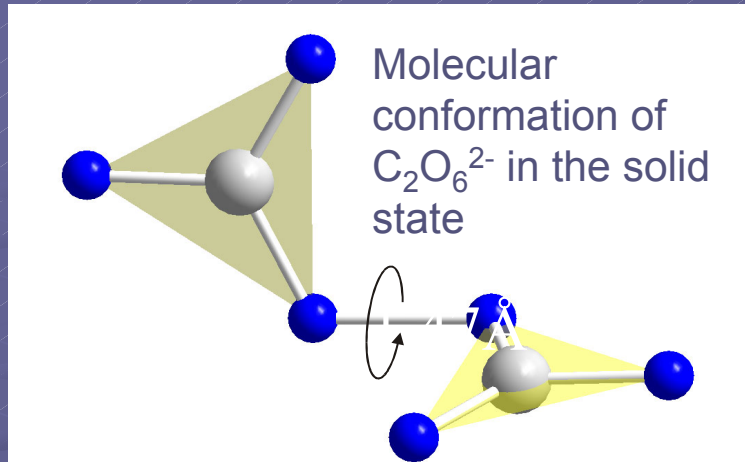
Thermal behavior of rubidium oxalate



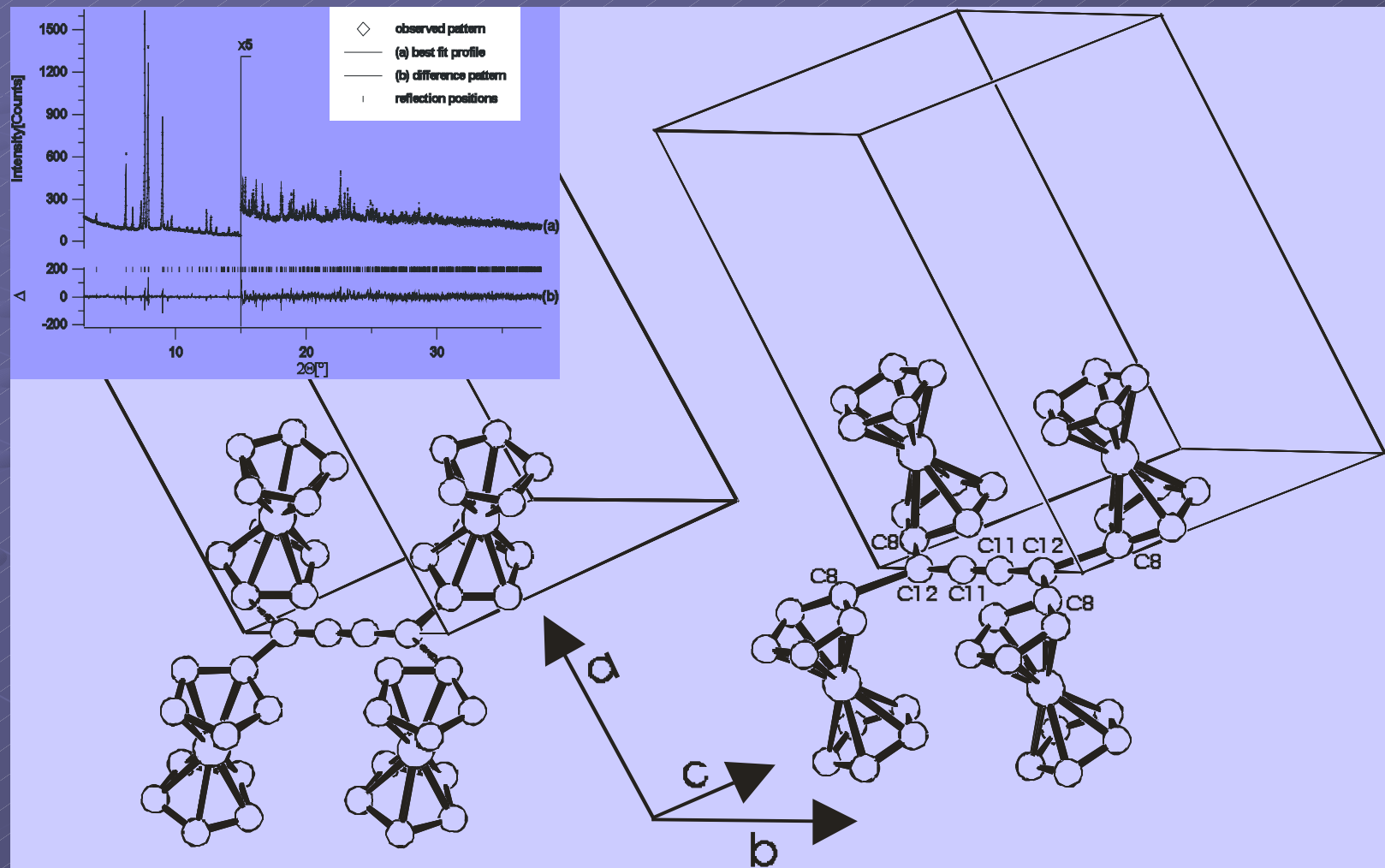
Time between scans: 120 sec (exposure time 30 sec, readout + erase time 90 sec)

25°-450°-25: 2°/60 sec; 200 scans (= 400 min)

The peroxydicarbonate dianion in $K_2C_2O_6$

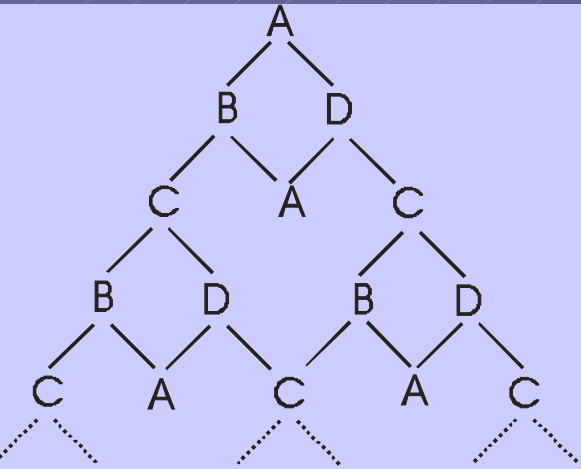


Tetraferrocenyl-[3]-Cumulene (Fc_2) $_2$ C-C-C-C(Fc_2) $_2$

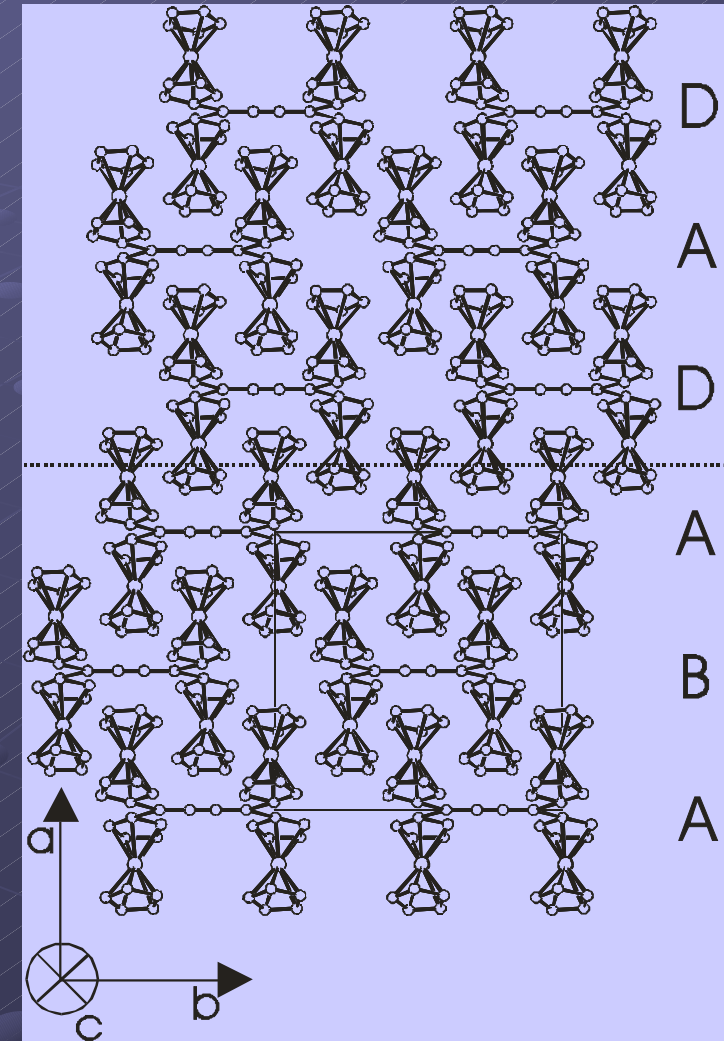
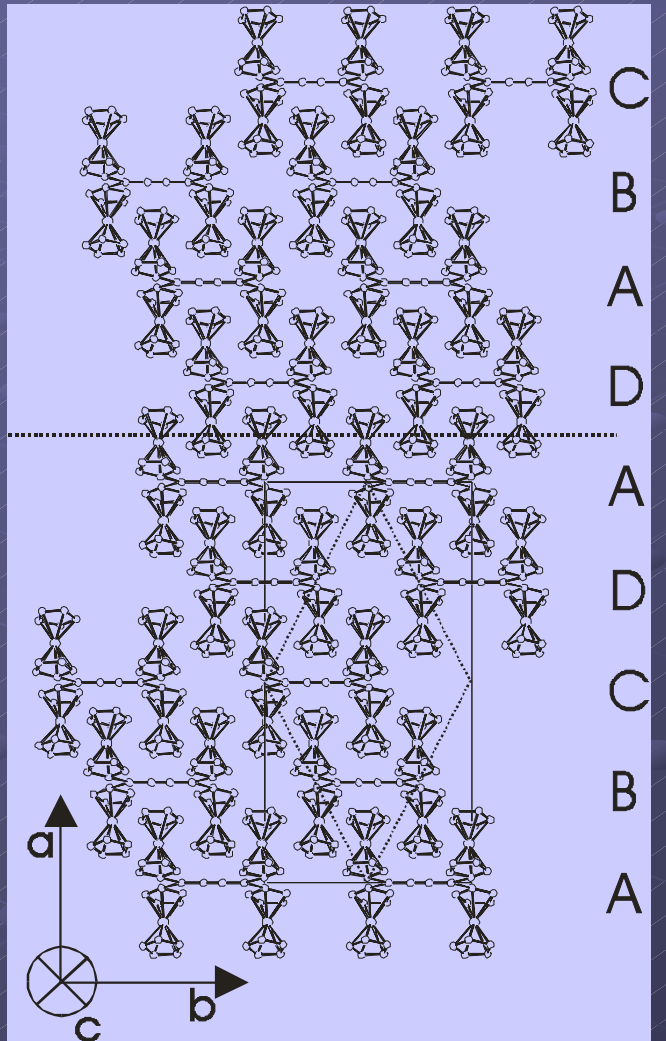


Crystal structure of the small unit cell (disordered model) of Tetraferrocenyl-[3]-Cumulene.

Tetraferrocenyl-[3]-Cumulene (Fc_2) $_2$ C-C-C-C(Fc_2) $_2$



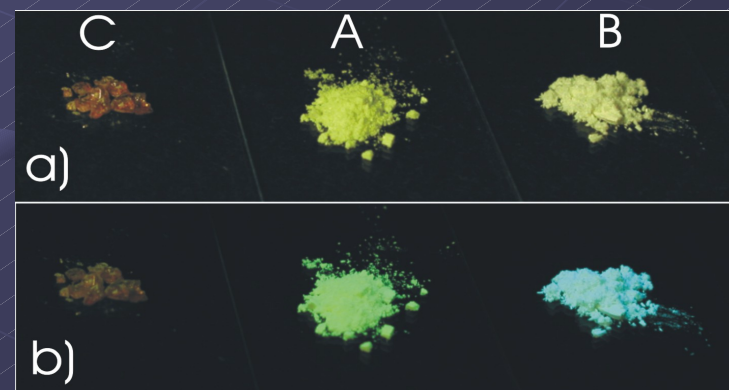
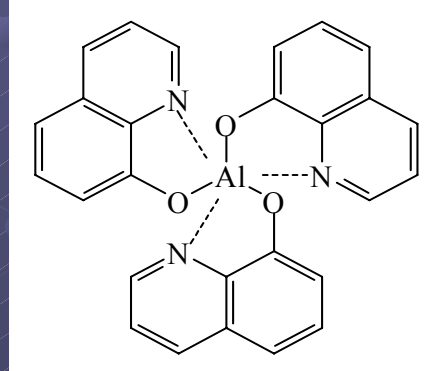
Tree like representation
of all allowed
combinations of layers up
to the forth period for
tetraferrocenyl-[3]-
cumulene starting from
layer A.



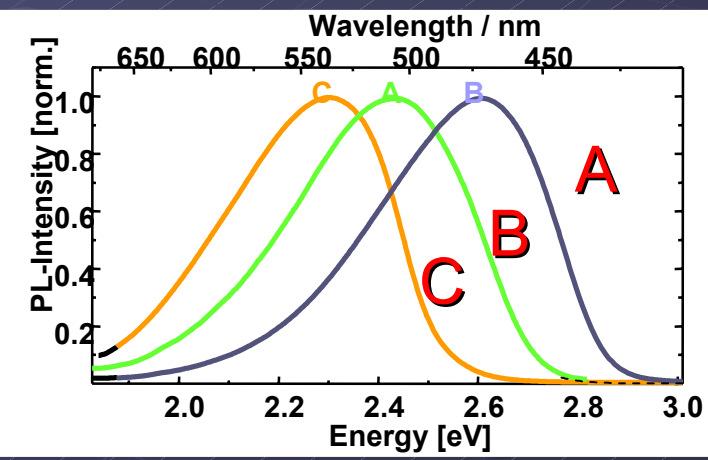
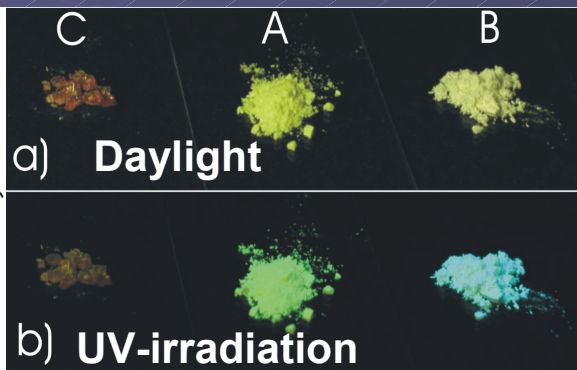
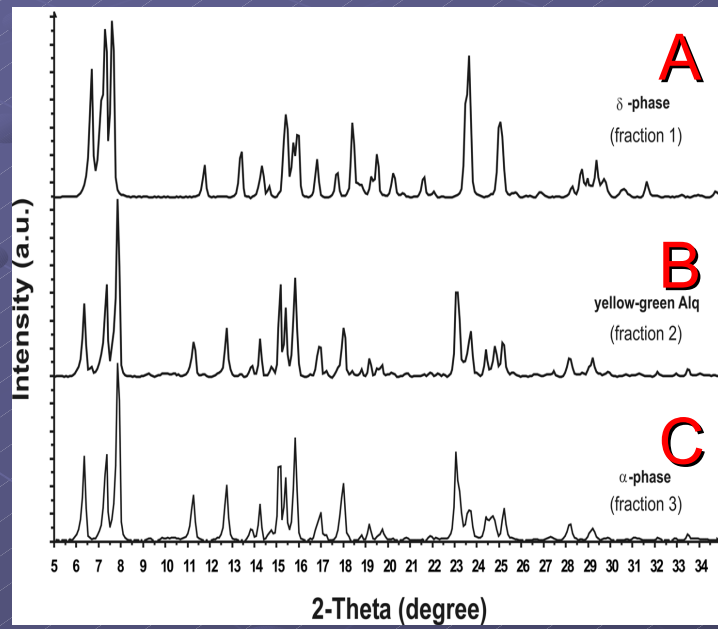
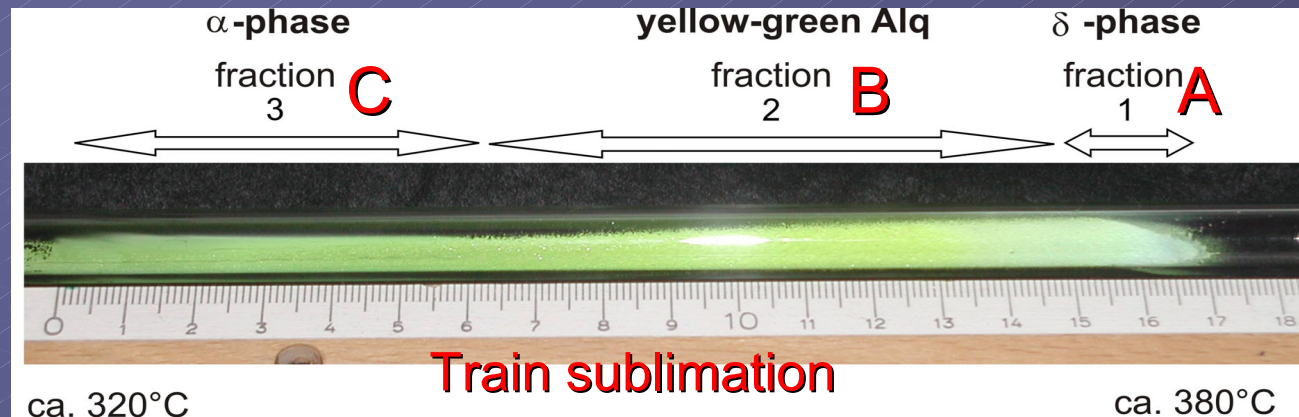
Plausible stacking fault models for Tetraferrocenyl-[3]-Cumulene
(ABCDA[DABC]), (ABA[DAD])

Evidence for the facial isomer in the blue luminescent δ -phase of tris(8-hydroxyquinoline)aluminum(III) (Alq_3)

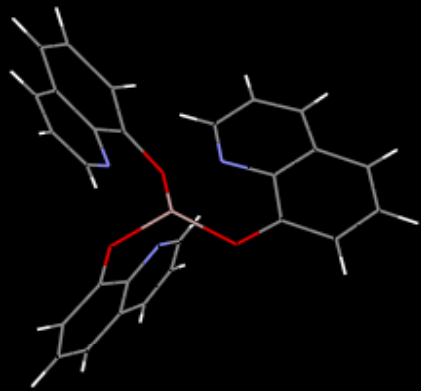
Michael Cölle, Robert E. Dinnebier and Wolfgang Brütting
Chem. Comm, 2002, 23, 2908-2909



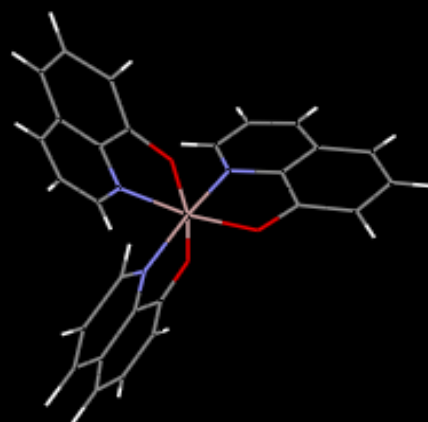
Properties of Alq₃



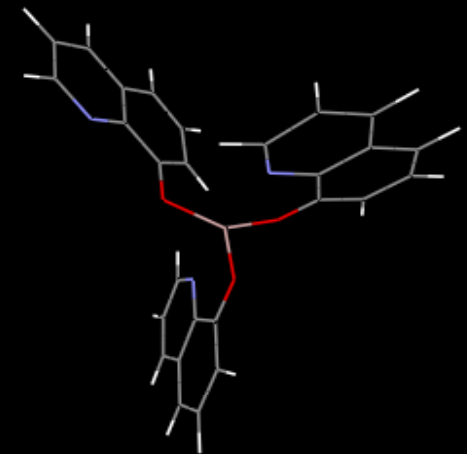
Isomers of δ -Alq₃



facial



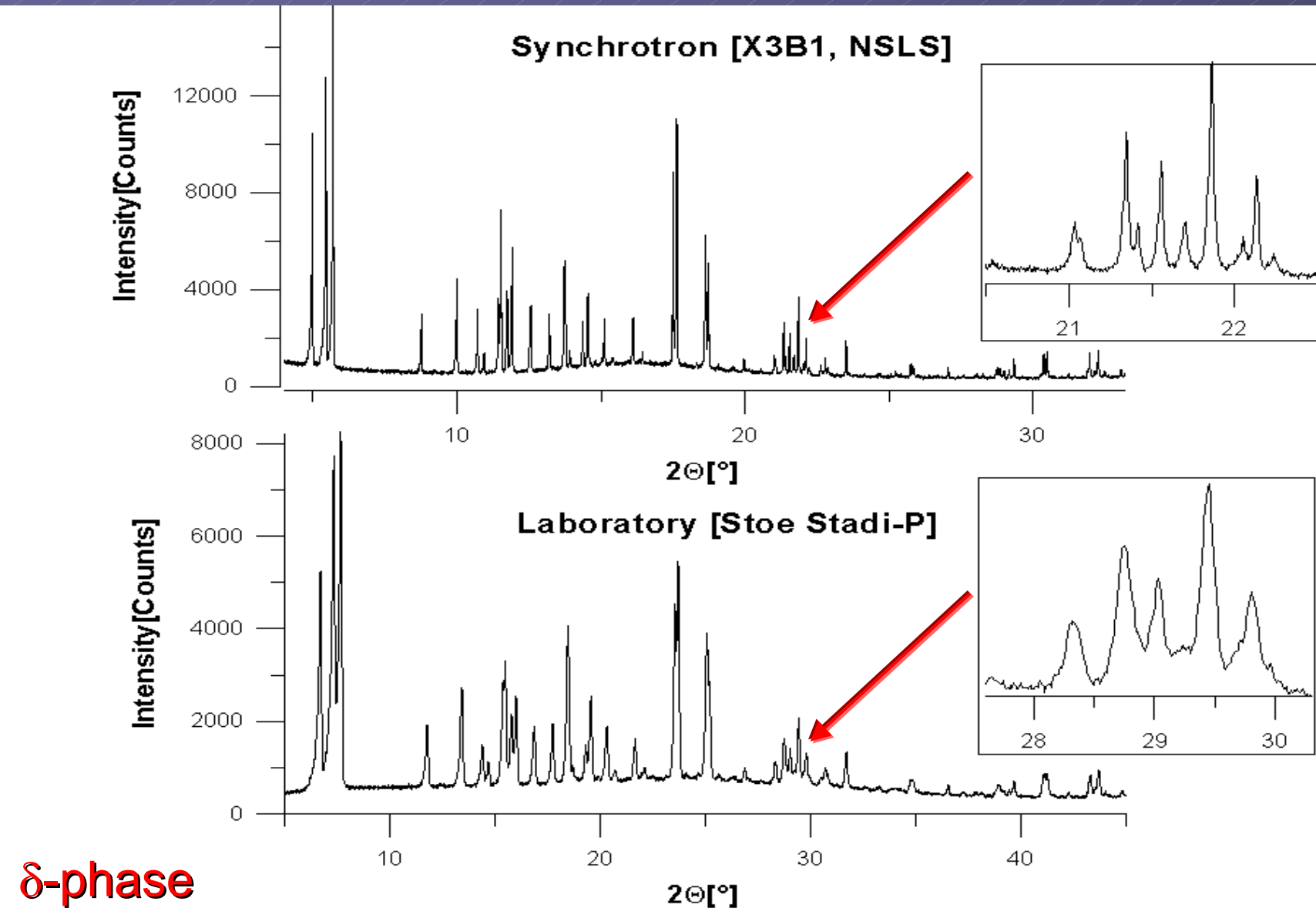
meridonal



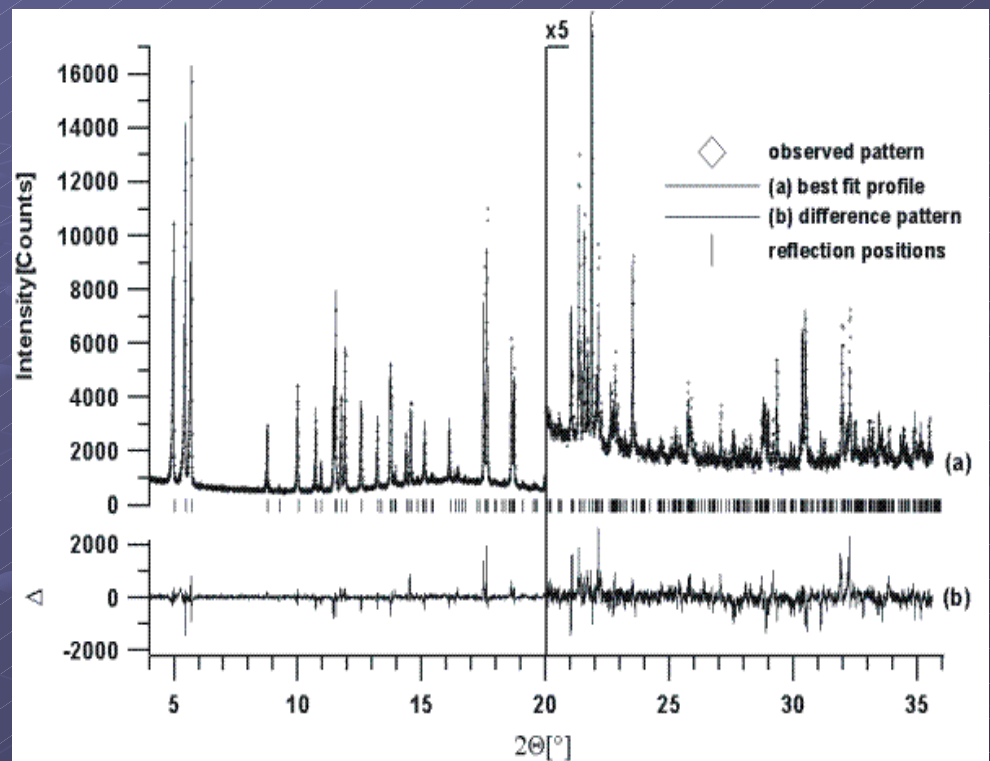
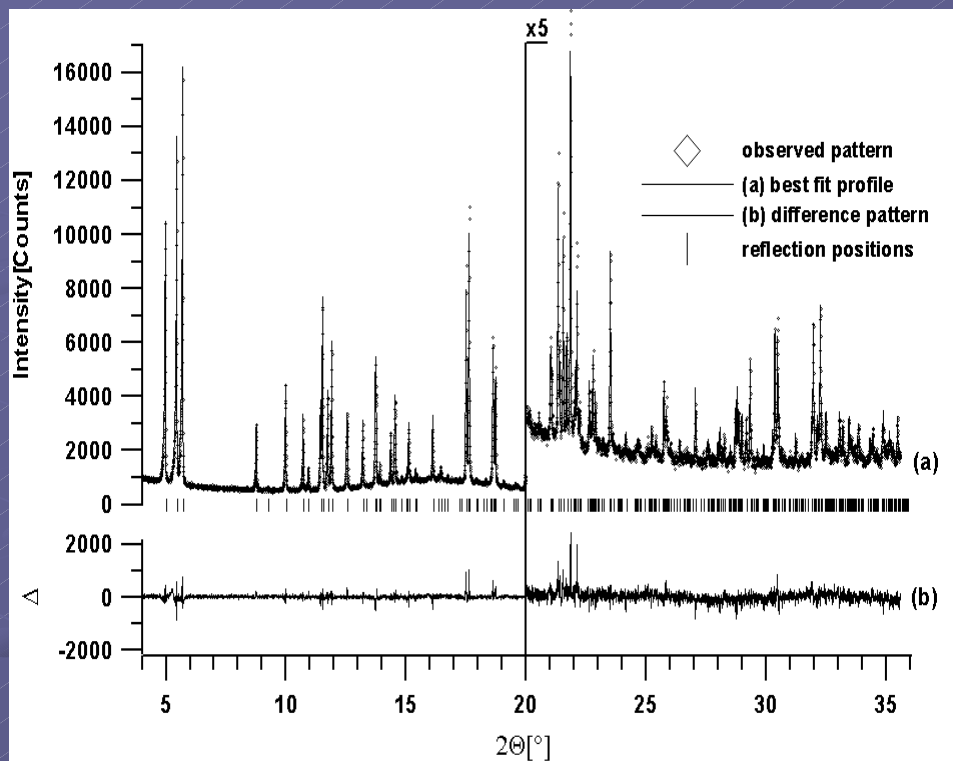
„meridonal-trans“

Different degrees of overlap of the π -orbitals of hydroxyquinoline ligands belonging to neighboring Alq₃ molecules are likely to be the origin of the significantly different electro-optical properties. Three isomers in the blue luminescent δ -phase of Alq₃ are possible

X-Ray Analysis of δ -Alq₃

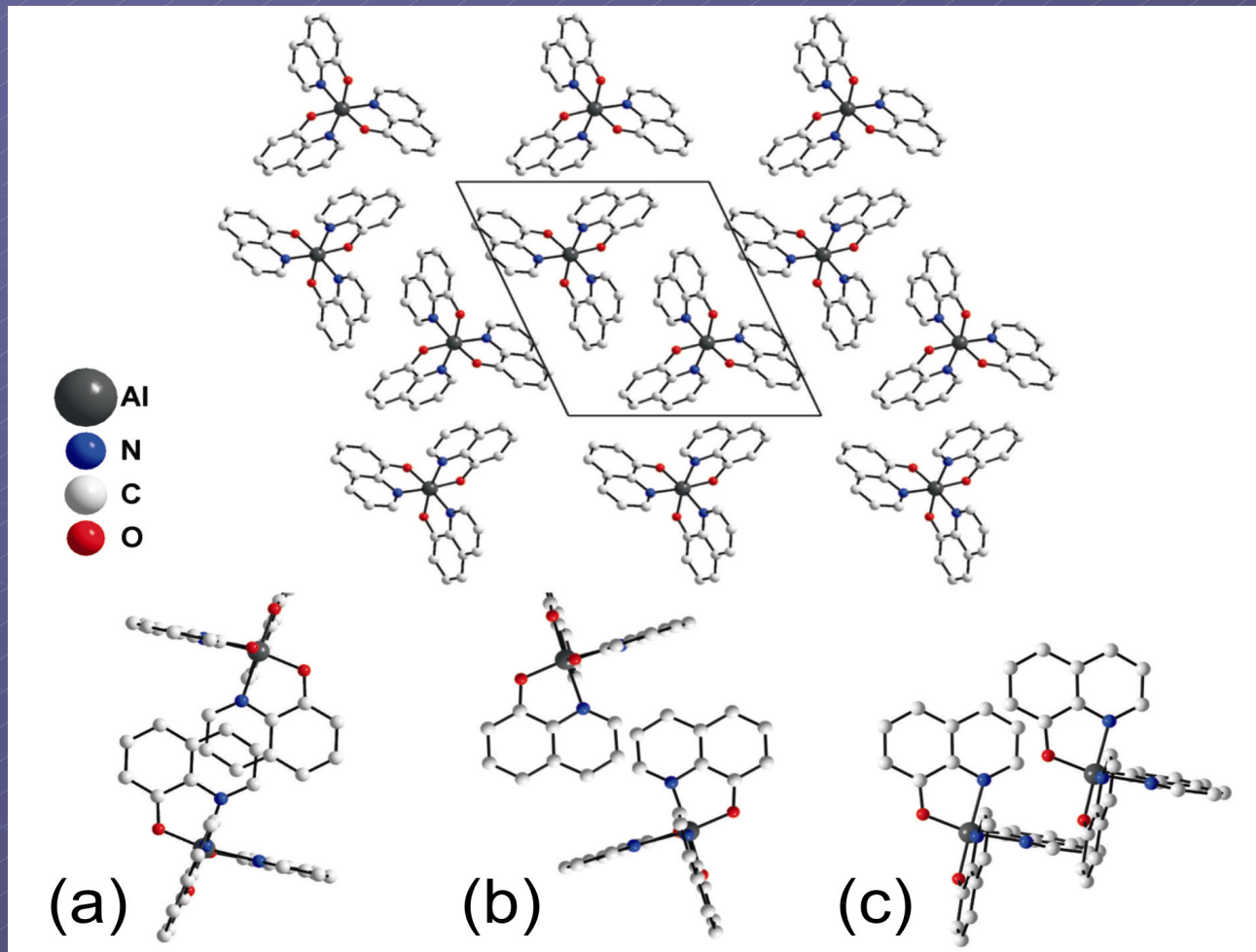


δ -Alq₃



Rietveld plots of δ -Alq₃ at ambient conditions The wavelength was $\lambda = 1.15 \text{ \AA}$.
Left: “correct” structure with facial isomer ($R_p = 5.0\%$, $R_{wp} = 6.5\%$, $R-F^2 = 10.5\%$)
Right: “false” structure with meridonal isomer ($R_p = 7.3\%$, $R_{wp} = 9.4\%$, $R-F^2 = 19.4\%$)

δ -Alq₃



Crystal structure of δ -Alq₃ in a projection along the c-axis. (a), (b) and (c) are projections perpendicular to the planes of the hydroxy-quinolineligands 1, 2 and 3, respectively, showing the overlap between ligands of neighbouring Alq₃ molecules.

Acknowledgement

Beamtime

High Resolution Powder Beamline X3B1 (NSLS)

High Resolution Powder Beamline BM16 (ESRF)

High Energy Beamline ID15 (ESRF), X17B (NSLS)

High Pressure Beamlines ID9 + ID30 (ESRF)

Chemistry Beamline X7B (NSLS)

High Resolution Powder Beamline B2 (HASYLAB)

Cooperation

Martin Jansen (MPI, Stuttgart)

Peter W. Stephens (SUNY at Stony Brook & X3B1, NSLS)

Sander van Smaalen, Martin Schneider, Markus Wunschel (U. of Bayreuth)

Poul Norby (U. of Oslo)

Falk Olbrich (U. of Magdeburg)

Robert Von Dreele (Los Alamos Natl. Lab.)

Matthias Wagner (U. of Frankfurt)

Wayne Dollase (U. of Los Angeles)

S. Kirik (U. of Krasnoyarsk) ...

Funding

*MPG, U. of Bayreuth, DFG, FCI, BMFT, INTAS,
Clariant GmbH, BASF AG, Böhringer Ingelheim KG*